Band gap formation in commensurate twisted bilayer graphene/hBN moiré lattices

A. Rothstein [1,2,*] C. Schattauer,[3] R. J. Dolleman,[1] S. Trellenkamp,[4] F. Lentz,[4] K. Watanabe [5] T. Taniguchi,[6] D. M. Kennes,[7,8] B. Beschoten [1] C. Stampfer [1,2,†] and F. Libisch [3,‡]

[1]*JARA-FIT and 2nd Institute of Physics, RWTH Aachen University, 52074 Aachen, Germany*
[2]*Peter Grünberg Institute (PGI-9), Forschungszentrum Jülich GmbH, 52425 Jülich, Germany*
[3]*Institute for Theoretical Physics, TU Wien, 1040 Vienna, Austria*
[4]*Helmholtz Nano Facility, Forschungszentrum Jülich GmbH, 52425 Jülich, Germany*
[5]*Research Center for Electronic and Optical Materials, National Institute for Materials Science, 1-1 Namiki, Tsukuba 305-0044, Japan*
[6]*Research Center for Materials Nanoarchitectonics, National Institute for Materials Science, 1-1 Namiki, Tsukuba 305-0044, Japan*
[7]*Institute for Theory of Statistical Physics, RWTH Aachen University, and JARA Fundamentals of Future Information Technology, 52062 Aachen, Germany*
[8]*Max Planck Institute for the Structure and Dynamics of Matter, Center for Free Electron Laser Science, 22761 Hamburg, Germany*

(Received 18 September 2023; revised 6 February 2024; accepted 20 March 2024; published 12 April 2024)

We report on the investigation of periodic superstructures in twisted bilayer graphene (tBLG) van der Waals heterostructures, where one of the graphene layers is aligned to hexagonal boron nitride (hBN). Our theoretical simulations reveal that if the ratio of the resulting two moiré unit-cell areas is a simple fraction, the graphene/hBN moiré lattice acts as a staggered potential, breaking the degeneracy between tBLG AA sites. This leads to additional band gaps at energies where a subset of tBLG AA sites is fully occupied. These gaps manifest as Landau fans in magnetotransport, which we experimentally observe in an aligned tBLG/hBN heterostructure. Our study demonstrates the identification of commensurate tBLG/hBN van der Waals heterostructures by magnetotransport, highlights the persistence of moiré effects on length scales of tens of nanometers, and represents an interesting step forward in the ongoing effort to realize designed quantum materials with tailored properties.

DOI: 10.1103/PhysRevB.109.155139

I. INTRODUCTION

The periodic structure of a crystalline solid is a key factor for its electronic band structure and hence its electrical and optical properties. The periodic potential leads to Bloch states as solutions of the Schrödinger equation [1] and to the formation of band gaps, well-known cornerstones of solid state physics. In conventional crystalline solids, the modulation of the periodic potential is fixed at the atomic scale. However, progress has been made to engineer artificial lattices, both at the atomic and nanoscale, to control electronic band structures, topological material properties, and exotic quantum phases in solids [2–7]. A remarkable class of such engineered solids are two-dimensional (2D) van der Waals materials with moiré lattices, where a small lattice misalignment or twist angle between two layers results in particularly large unit cells, orders of magnitude larger than the underlying crystal lattice constant [8].

A prominent example of such a 2D van der Waals material is twisted bilayer graphene (tBLG) [Fig. 1(a)]. In tBLG, two layers of graphene are stacked with a small twist angle, creating a moiré lattice with a large periodic modulation on the order of several nanometers. The periodic modulation localizes the electronic wave function on sites where the carbon atoms of the individual graphene layers align within the trigonal tBLG moiré lattice (known as AA sites), leading to the formation of additional band gaps [9]. Near the so-called magic angle of 1.1°, tBLG shows a wealth of interesting quantum phases, including superconductivity, correlated insulators, and orbital magnetism, all of which depend sensitively on the flat electronic bands in this system [10–22]. Furthermore, tBLG can be combined in a single van der Waals heterostructure with a second moiré lattice formed by aligning the crystallographic axes of one of the graphene layers with one of the encapsulating hexagonal boron nitride (hBN) layers, exploiting the small lattice constant mismatch between these two materials [23–28]. In this case, an overall *composite* supermoiré lattice is formed [29–31], which breaks the inversion symmetry of tBLG, leading to an altered electronic structure [32–36], and to the emergence of novel phases such as ferromagnetism [18,19,37–39] or anomalous quantum Hall states [19,34].

In this work we present a theoretical model for commensurate tBLG/hBN heterostructures and show that, in the special case where the ratio of the areas of the unit cells of tBLG and of the graphene/hBN (gr/hBN) moiré lattice form a simple fraction, the degeneracy of the AA sites of the tBLG is lifted in a periodic manner, which leads to a stronger localization of the electronic wave function on a subset of the tBLG AA

*alexander.rothstein@rwth-aachen.de
†stampfer@physik.rwth-aachen.de
‡florian.libisch@tuwien.ac.at

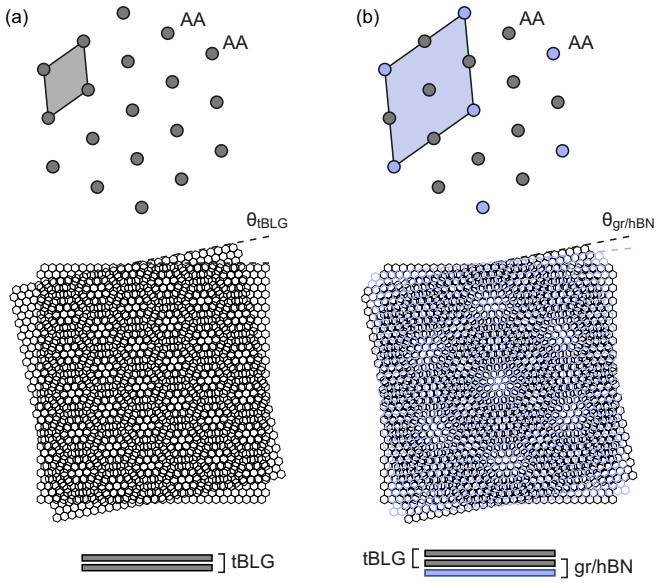

FIG. 1. (a) Schematic representation of a tBLG moiré lattice. Gray circles represent the AA sites while the gray rhombus denotes the tBLG unit cell. (b) Schematic representation of a composite supermoiré lattice consisting of a tBLG moiré lattice [same as in (a)] and a graphene/hBN (gr/hBN) moiré lattice. Blue circles represent the AA sites of the resulting supermoiré lattice. The shaded rhombus denotes the corresponding supermoiré unit cell.

sites. This results in turn in a further flattening of the bands of tBLG and in the appearance of additional band gaps, which manifest themselves as Landau fans at fractional filling factors in the magnetotransport characteristic of the system. This prediction is confirmed experimentally by magnetotransport measurements in a tBLG sample aligned to hBN. Remarkably, the additional band gaps are not related to full filling of a specific (super)moiré cell but to the filling of a *subset* of AA sites of the tBLG, selected by the graphene/hBN moiré lattice.

II. THEORETICAL MODEL OF tBLG MOIRÉ SYSTEMS

The theoretical modeling of tBLG [see Fig. 1(a)] involves large unit cells, e.g., about 13×10^3 atoms for a twist angle of approximately 1°. For tBLG, we parametrize our model directly from density functional theory (DFT), by evaluating the relative, local stacking configurations of the carbon atoms in the top and bottom graphene layers [40]. Using the local DFT parametrization, we assemble a tight-binding Hamiltonian of the entire tBLG moiré unit cell. Given the different energies of the different stacking configurations, the two layers will stretch and corrugate to minimize their energy. We account for this relaxation and for the resulting strain by a membrane model [41]. We efficiently describe transport through such a system by considering a ribbon geometry of finite width W in one direction (y direction) [40]. We choose $W \approx 210$ nm (corresponding to 15 tBLG moiré unit cells) to reduce finite-size effects (for further details see Appendix E). The band structure of the modeled tBLG ribbon features a number of quite flat, nearly degenerate bands close to the charge neutrality point at $E = 0$ meV [Fig. 2(a)]. The corresponding density of states (DOS) shows the expected peak around charge neutrality. The energy of the flat bands is confined to a narrow energy interval delimited by the $\nu = \pm 4$ band insulating states [see arrows in Fig. 2(a)] (note that our single-particle model does not include correlation effects, and therefore no further interaction-induced gaps are visible). For small fillings, the spatial distributions of the charge carrier density shows the expected localization on the AA sites of the tBLG moiré lattice [Fig. 2(b)]. According to this localization on a regular triangular lattice, each tBLG moiré unit cell contains a total of four charge carriers due to the spin and valley degeneracy, and a band gap opens at full filling of all AA lattice sites [9,42].

III. THEORETICAL MODEL OF tBLG/hBN COMPOSITE MOIRÉ SYSTEMS

Including into the model the graphene/hBN moiré lattice poses a further challenge, as the additional alignment between one graphene layer and the hBN substrate results in an even larger overall composite supermoiré unit cell [see Fig. 1(b)]. This applies already to the parametrization by DFT: using the same approach as for tBLG alone would require many additional DFT calculations for all possible shifts between the two graphene layers and all possible alignments of the additional hBN layer. To alleviate this further parametrization effort, we only consider the tBLG parameters from DFT, and add the graphene/hBN moiré lattice based on an effective potential approach [43]. We use DFT to derive slowly varying, effective potentials that describe the local modulations induced by the graphene/hBN moiré lattice in the tBLG. Describing the short-range variations induced by the alternating boron and nitrogen atoms requires short-range components of the effective potential, modeled by a second potential with opposite signs on the two sublattices of the graphene layer in contact with the hBN [44,45]. This combination of a smooth and an alternating potential allows us to model the influence of the hBN alignment and to introduce the length scale of the graphene/hBN moiré lattice into the tBLG Hamiltonian in an easily adaptable manner. We have verified numerically that this effective potential approach leads to qualitatively similar predictions (concerning the additional satellite Landau levels, single-particle band gaps etc.) as the full DFT-based atomistic parametrization of the graphene/hBN moiré lattice. While our ribbon geometry allows, in principle, incommensurate unit-cell sizes perpendicular to the ribbon, we impose a periodic cell of moderate size in x direction along the ribbon. For a tBLG twist angle of $\theta_{\mathrm{tBLG}} = 0.987^\circ$ and a graphene/hBN twist angle of $\theta_{\mathrm{gr/hBN}} = 0.62^\circ$, both unit cells feature one identical spatial dimension, which we orient in x direction of our ribbon geometry. A suitable shift of the hBN layer then allows to obtain a supermoiré cell with comparatively small periodicity of 24.8 nm in the x direction. This supermoiré cell features roughly 8×10^4 carbon atoms, and an area of roughly 300 nm^2. The 15 tBLG moiré unit cells in the y direction, perpendicular to the transport direction, correspond to 20 graphene/hBN moiré unit cells. The areas of these two single moiré unit cells thus are commensurate, with $A_{\mathrm{tBLG}}/A_{\mathrm{gr/hBN}} = \frac{20}{15} = \frac{4}{3}$, i.e., the resulting supermoiré unit cell contains three (four) tBLG (graphene/hBN) moiré unit cells (see Appendix E).

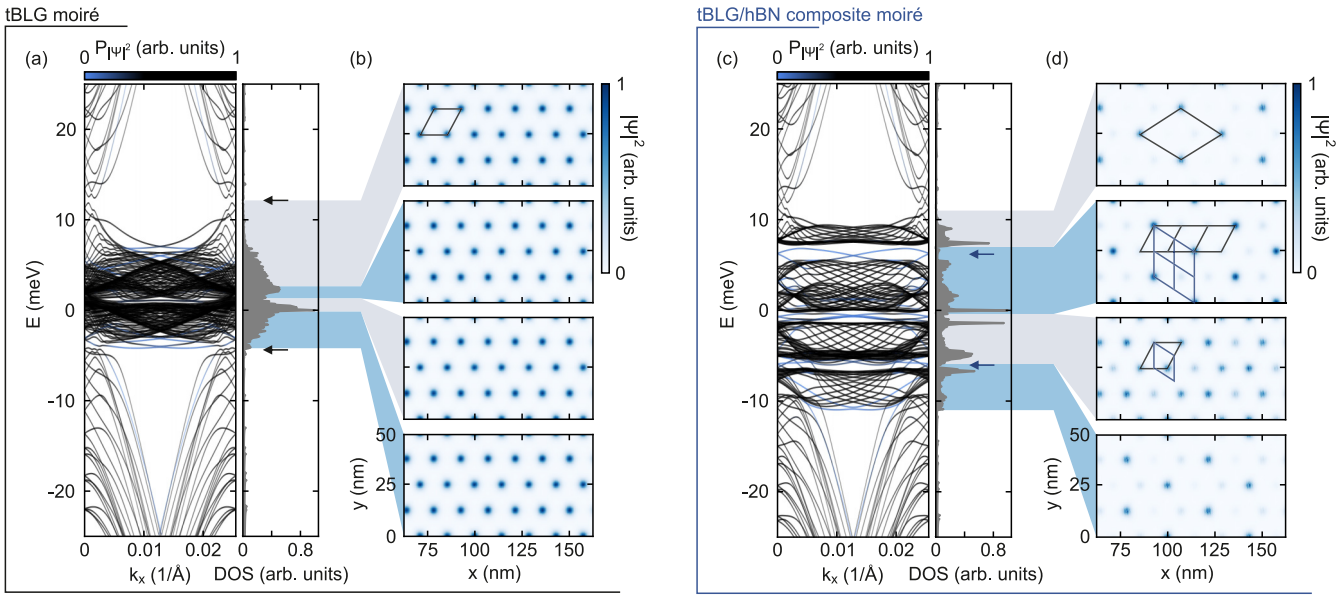

FIG. 2. (a) Band structure and density of states calculation of a tBLG moiré system at a twist angle of $\theta_{\mathrm{tBLG}} = 0.987^\circ$ (black arrows mark the tBLG moiré-induced single-particle band gaps). To distinguish bulk from edge states in our ribbon geometry (width $W \approx 210$ nm), we color each line according to the probability $P_{|\Psi|^2}$ to find the Bloch state at the center of the ribbon, i.e., within $[0.2, 0.8] \times W$. (b) Spatial distribution of the charge carrier density in one graphene layer, averaged over different energy windows (shaded areas). The charge carrier density accumulates at the AA sites located at the corners of the tBLG moiré unit cell (see sketched rhombus) forming a uniform triangular lattice in real space. One tBLG moiré unit cell contains one AA site (proportional contributions from the corners). The y axis is identical for all panels. (c), (d) Same as in (a) and (b) but with an additional hBN alignment of $\theta_{\mathrm{gr/hBN}} = 0.62^\circ$. Blue arrows mark the positions of the additional gaps forming due to the hBN alignment. Black rhombus in the upmost panel represents the unit cell of the supermoiré lattice defined by the tBLG and the graphene/hBN moiré lattices. The supermoiré unit cell contains a total of 3 AA sites. On this scale three tBLG moiré unit cells feature the same area as four graphene/hBN moiré unit cells (second panel from top). The presence of the graphene/hBN moiré strongly modulates the electron density on the different AA sites of the tBLG moiré lattice.

A. Influence of the graphene/hBN moiré lattice to the tBLG system

The graphene/hBN moiré lattice induces interactions between the tBLG moiré flat bands, breaking their degeneracy since adjacent tBLG moiré unit cells now feature different alignments with the graphene/hBN moiré lattice. The resulting level repulsion between the flat bands causes a pronounced broadening of the flat band region [compare Figs. 2(a) and 2(c)], enhancing the asymmetry of the $\nu = \pm 4$ band gaps. The DOS for the composite system features a much broader region of peaks, with substantial substructures, delimited by the two band gaps of the bulk tBLG moiré lattice excluding the edge states [see Fig. 2(c)].

To further understand the effects of the commensurate graphene/hBN moiré lattice, we investigate the spatial distribution of the charge carrier density. Because the charge occupation of the triangular lattice of AA sites in the original tBLG is uniform [Fig. 2(b) and line cuts in Fig. 3(a)], the resulting filling factor corresponds to four charge carriers per AA site (due to the spin and valley degree of freedoms). The situation is different in the presence of the commensurate graphene/hBN moiré lattice [Figs. 2(c) and 2(d)]. In this case, we observe an additional band gap at an energy of approximately $|E| \approx \pm 7$ meV [see blue arrows in Fig. 2(c)]. Considering the distribution of charge carrier density $|\psi|^2$, we find the occupation of the three AA sites within the supermoiré unit cell is now no longer uniform [see shaded regions in Fig. 2(c) and density plots in Fig. 2(d) as well as the corresponding line cuts in Fig. 3(b)]. The newly induced energy gap separates energy regions with varying occupation of the three tBLG AA sites [Fig. 2(d)]. In particular, only one out of the three AA sites is occupied in the range from 7 to 11 meV and from -6 to -11 meV [Fig. 2(d), top and bottom pictures]. Indeed, when counting the number of bands above and below the additional gap, we find that one third of the moiré flat bands lies above the new gap. In magnetotransport, this gap should appear as an additional Landau fan at a filling of two out of three states, or $\nu_{\mathrm{sat}} \approx \pm 4 \times 2/3 = \pm 2.67$.

B. Magnetotransport simulation

We simulate the magnetotransport behavior of the tBLG and the tBLG/hBN systems based on the associated band structure. To investigate the dependence on magnetic field B, we use a Peierl's substitution to include the corresponding gauge phase in each hopping in the tight-binding model. For the Bloch states we extract the group velocities $v_n(E) = (1/\hbar)\,\partial E_n(k, B)/\partial k$. We then calculate the magnetoconductance by summing at a fixed energy over all available modes with positive group velocity $v_n(E) > 0$ (i.e., the right-moving modes, summing over all modes would result in zero due to time-reversal symmetry), weighted by the respective group

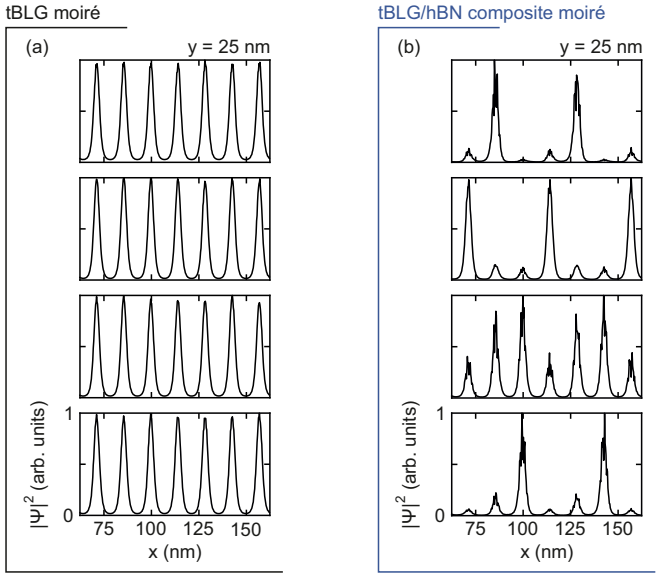

FIG. 3. (a) Line cuts of the charge carrier density distribution averaged over specific energy ranges as shown in Fig. 2(b) for $y = 25$ nm of the tBLG system. The energy ranges are given by $E_1 \in [2.5, 12]$ meV, $E_2 \in [1.3, 2.5]$ meV, $E_3 \in [-0.153, 1.3]$ meV, and $E_4 \in [-4.2, -0.153]$ meV. The charge distribution on the different AA sites is uniform for tBLG. The y axis is identical for all panels. (b) Same as in (a) but with the additional hBN alignment of $\theta_{\mathrm{gr/hBN}} = 0.62^\circ$ [line cuts are taken from corresponding panels in Fig. 2(d)]. The energy ranges are given by $E_1 \in [11, 7]$ meV, $E_2 \in [-0.4, 7]$ meV, $E_3 \in [-6, -0.4]$ meV, and $E_4 \in [-11, -6]$ meV. The presence of the graphene/hBN moiré lattice strongly modulates the electron density on the tBLG AA sites.

velocity of the underlying Bloch states [40] (see Appendix F for a derivation)

$$G(E) = \frac{e^2}{h}\frac{\mathrm{d}}{\mathrm{d}E}\sum_{\substack{n:\, v_n(E)>0 \\ E_n<E}} \hbar v_n(E)\Delta k \equiv R^{-1}(E), \qquad (1)$$

where Δk is the k-point spacing of the band structure (we use 5760 k points for the Brillouin zone with a size of 0.25 nm^{-1}). We compare the magnetoresistance $R(E)$, obtained by inverting Eq. (1), of the bare tBLG in Fig. 4(a) to the case of tBLG/hBN in Fig. 4(b) as a function of the filling factor ν and normalized magnetic flux per tBLG moiré unit cell (uc) $\phi = \Phi_{\mathrm{uc}}/\Phi_0$, where $\Phi_0 = h/e$ is the magnetic flux quantum (ν and ϕ are thus both defined with respect to the tBLG unit cell). In both cases, the band gaps caused by the tBLG moiré lattice give rise to Landau fans at integer fillings $\nu = \pm 4$, i.e., at full filling of four charge carriers per tBLG moiré unit cell. In the case of tBLG/hBN in Fig. 4(b) the expected additional set of Landau fans emerge from the band gaps induced by the supermoiré structure at noninteger filling $\nu \approx \pm 2.67 \equiv \nu_{\mathrm{sat}}$ (see arrows in Fig. 4). In our single-particle calculations, this fractional filling (of two out of three AA sites times 4) emerges because the graphene/hBN moiré potential acts as a staggered potential and breaks the degeneracy of the AA sites within the supermoiré unit cell. Crucially, in order to observe an additional band gap at full filling of a selected subset of AA sites, we need the very same partitioning of AA sites in each supermoiré unit cell, so we require a *commensurate* moiré supercell.

C. General selection rule

To generalize our discussed model we consider a commensurate supermoiré structure consisting of l tBLG moiré unit cells and m graphene/hBN moiré unit cells (l, m both integers), so that the area of the supermoiré unit cell is given by $lA_{\mathrm{tBLG}} = mA_{\mathrm{gr/hBN}}$. If the graphene/hBN moiré lattice selects a subset p of the l tBLG AA sites within the overall supermoiré lattice, we expect the appearance of an additional band gap and the accompanying Landau fan at a noninteger filling factor of

$$\nu_{\mathrm{sat}}(l, p) = 4\frac{p}{l} = 4\frac{pA_{\mathrm{tBLG}}}{mA_{\mathrm{gr/hBN}}}, \qquad p < l. \qquad (2)$$

The geometry of the model system we considered above defines $l = 3$ and $m = 4$. In the corresponding supermoiré unit cell, one of the three tBLG AA sites is directly aligned with an AA site of the graphene/hBN moiré lattice below, and thus differs from the other two tBLG AA sites (see Appendix G). This observation suggests that the threefold-degenerate AA sites of the unperturbed tBLG are split into a doublet and a singlet. Consequently, possible values for p are either $p = 1$ or 2, depending on whether the final energy of the single hBN-aligned tBLG AA site or the two other non-hBN-aligned tBLG AA sites is lower. The hBN-aligned tBLG AA site is less energetically favorable [45], suggesting that the doublet is filled first, and thus $p = 2$. Indeed, the numerical value $\nu_{\mathrm{sat}} \approx 2.67$ is consistent with $p = 2$ for our model system, as $\nu_{\mathrm{sat}}(3, 2) = 4 \times 2/3 \approx 2.67$ according to Eq. (2).

We find that the appearance of an additional gap is robust with respect to different twist angles of the tBLG moiré lattice (see Appendix F). The geometric constraints of a periodic, commensurate moiré lattice allow only for a limited set of combinations of l and m (see Appendix G). In general, we expect values of l and m to be limited by the experimentally realizable size of a regular supermoiré lattice, as otherwise twist-angle inhomogeneities would wash out any additional Landau fans (see Appendix D). The associated fraction p/l depends on the specific details of the (staggered) potential induced by the graphene/hBN moiré lattice within the tBLG, and the relative geometrical orientation of the two moiré lattices [46]: The energetic shift due to the presence of the graphene/hBN moiré lattice originates from its three high-symmetry sites with local energetic shifts [45]; the exact value of p/l will therefore depend on the precise relative alignment of these sites with the AA sites of the tBLG moiré lattice.

IV. EXPERIMENTAL OBSERVATION

Next, we turn to transport experiments which show that a Landau fan can indeed be observed at a noninteger filling factor, conclusively due to commensurate tBLG/hBN moiré lattices. In a four-terminal setup, we investigate a tBLG/hBN Hall bar device at a temperature of $T \approx 30$ mK (see Appendices A1–A4 for details on the fabrication and further experimental characterization) and perform magnetotransport measurements which we compare to theory (see Figs. 4 and

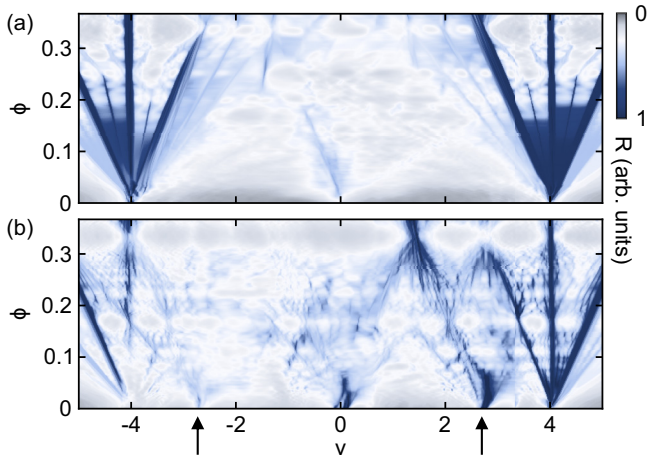

FIG. 4. (a) Magnetoresistance R [see Eq. (1)] simulation of a tBLG system with a twist angle of $\theta_{\mathrm{tBLG}} = 0.987^{\circ}$. Landau levels emerge from the charge neutrality point ($\nu = 0$) and the single-particle band gaps at full filling of the tBLG moiré lattice unit cell ($\nu = 4$). (b) Same as in (a) but for a composite tBLG/hBN system with an additional hBN alignment of $\theta_{\mathrm{gr/hBN}} = 0.62^{\circ}$. For this case there are additional Landau levels emerging from noninteger filling factors of ($\nu_{\mathrm{sat}} \approx \pm 2.67$) (see black arrows).

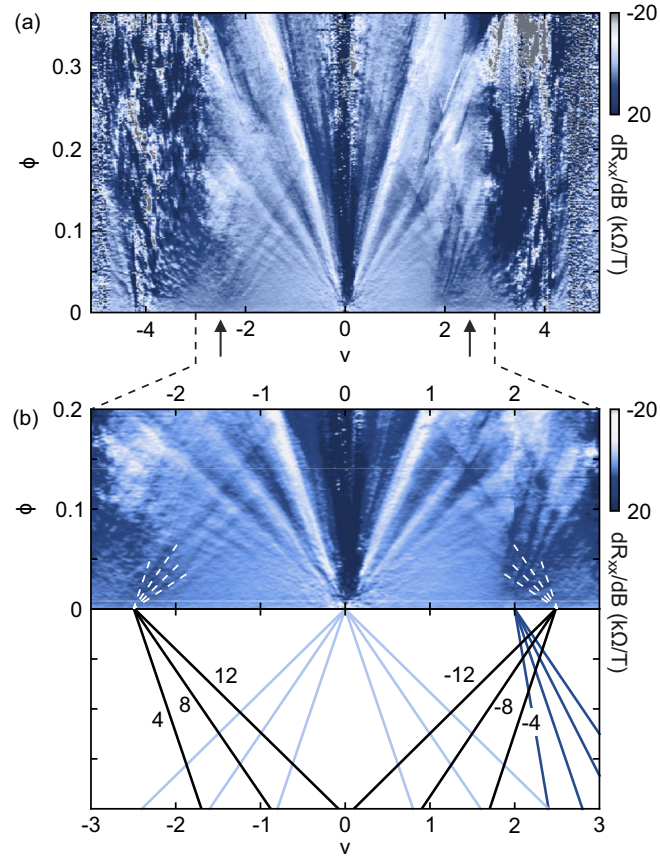

FIG. 5. (a) Magnetic field derivative of the longitudinal resistance as a function of the filling factor ν and normalized magnetic flux per tBLG moiré superlattice unit cell ϕ. We observe clear Landau levels emerging from charge neutrality and an integer filling factor of $\nu = 2$. The Landau levels emerging from $\nu = \pm 4$ are less pronounced. Furthermore, additional Landau levels emerging from a noninteger filling factor of around $\nu \approx \pm 2.5 \equiv \nu_{\mathrm{sat}}$ tilted towards the charge neutrality point are visible. (b) Zoom-in into the relevant area from (a). The lines are plotted as a guide to the eye to highlight relevant Landau fans at the charge neutrality point (light blue), the integer filling $\nu = +2$ (dark blue), and at the noninteger filling factor $\nu \approx \pm 2.5$ (black).

5). In Fig. 5(a), we show the derivative of the longitudinal resistance with respect to the magnetic field $\mathrm{d}R_{\mathrm{xx}}/\mathrm{d}B$ as a function of ν and ϕ (see Appendix D for a plot without the derivative along the magnetic field axis). We observe Landau fans emerging from the charge-neutrality point at $\nu = 0$, and the band-insulating states at $\nu = \pm 4$, as well as a set of Landau levels arising from the correlated insulator at $\nu = 2$, as it is expected for tBLG near magic angle [10,13]. In addition, we also observe a set of Landau fans emerging from noninteger fillings $\nu_{\mathrm{sat}} = \pm(2.50 \pm 0.11)$ [see Fig. 5(b); the fractional fillings where the additional feature occurs are marked by the black arrows]. If we attribute the additional Landau fans at filling ν_{sat} to full filling from a hypothetical moiré unit cell of size A_{hyp}, we would get $A_{\mathrm{hyp}} n_{\mathrm{sat}} = 4$, where n_{sat} is the charge carrier density where the Landau fan appears. In units of fillings of the tBLG moiré unit cell, this results in $A_{\mathrm{hyp}} = 4A_{\mathrm{tBLG}}/\nu_{\mathrm{sat}} = 1.6A_{\mathrm{tBLG}}$. Assigning this hypothetical moiré unit cell A_{hyp} to a graphene/hBN moiré unit cell yields a moiré wavelength of $\lambda_{\mathrm{hyp}}^{\mathrm{gr/hBN}} \approx 18.5$ nm, which is larger than the theoretical maximal value for a graphene/hBN moiré lattice of $\lambda_{\mathrm{gr/hBN}}^{\mathrm{max}} \approx 14.7$ nm [29], making this scenario impossible. Furthermore, the area A_{hyp} cannot correspond to any unit cell of the supermoiré lattice either since this would require an area of at least $2A_{\mathrm{tBLG}}$. We thus conclude that the observed Landau fans cannot be explained by full filling of a hypothetical cell size. Instead, the real-space selection rule described by Eq. (2) can easily explain the observed additional Landau fans.

The question remains whether the observed feature of additional Landau fans at fractional fillings is due to correlations. The phase diagram of twisted bilayer graphene is very complex, with a plethora of phenomena driven by many-body effects [47], some of which could give rise to fractional states. However, here we identify a number of key experimental features that are inconsistent with a many-body explanation: (i) The additional Landau fans extend over a wide density range from $\nu \approx \pm 2.5$ at $\phi = 0$ to $\nu \approx \pm 0.5$ at $\phi \approx 0.2$. In contrast, reports of correlation-driven Landau fans are extremely limited in carrier density (as correlated states emerge from the physics of specific fillings). The latter is particularly true for the many-body physics of fractional states [11,47]. (ii) The slope of the Landau fans we observe implies a Landau-level degeneracy of $\nu_{\mathrm{LL}} = -12, -8, -4, 4, 8, 12$, consistent with single-particle predictions but inconsistent with predictions from fractional many-body physics [47–50]. (iii) The features of the additional Landau fans emanating from the fractional filling cross through those from the charge-neutrality point without interruption, which is not expected for Landau levels emerging from correlated states in tBLG [16,51]. We therefore attribute these additional Landau fans to the presence of the graphene/hBN moiré lattice acting as a staggered potential

that selects a subset of tBLG AA sites within each supermoiré unit cell, as shown by the magnetotransport simulation [see Fig. 4(b)]. This also serves as a warning that additional Landau fans do not necessarily imply the emergence of correlated physics. Indeed, our mean-field tight-binding approach explains the resulting band gap at fractional fillings of the tBLG moiré lattice at ν_{sat} entirely based on an effective single-body Hamiltonian by the lifting of the degeneracies of the tBLG AA sites, in line with both experimental observations mentioned above.

To estimate the tBLG twist angle θ_{tBLG}, we determine the tBLG superlattice density from magnetotransport measurements to be $n_{\mathrm{s}} \approx \pm(2.17 \pm 0.06) \times 10^{12}\ \mathrm{cm}^{-2}$ and use $\theta_{\mathrm{tBLG}} = [\sqrt{3}n_{\mathrm{s}}/8]^{1/2}a$, where $a = 0.246$ nm is the graphene lattice constant [11]. This results in a value of $\theta_{\mathrm{tBLG}} \approx 0.97^{\circ} \pm 0.02^{\circ}$ (see Appendix B for further details). For the composite graphene/hBN moiré lattice, the discussion above suggests a filling of some fraction p/l of the AA sites within the supermoiré unit cell. However, since the filling factor ν_{sat} and the area of the tBLG moiré unit cell A_{tBLG} are the only experimental accessible quantities in Eq. (2), the size of the graphene/hBN moiré unit cell area is not uniquely determined by the measured filling ν_{sat}: it depends still on the fraction p/m (see Appendix B). Hence, there are triples of integers (l, m, p) which result in identical values for ν_{sat} but correspond to different angles $\theta_{\mathrm{gr/hBN}}$. This result might appear surprising, given that the filling at which moiré-induced Landau fans appear are usually precise indicators for the underlying moiré unit-cell areas and thus for the occurring twist angles. The underlying physical reason is that ν_{sat} is not directly determined by the size of the graphene/hBN moiré lattice, but rather by the degeneracy lifting induced by the graphene/hBN moiré lattice on the AA sites of the tBLG. Consequently, it highlights the importance of the discussed real-space effect and shows that great care must been taken by the interpretation of moiré-induced Landau fans. In particular, there are values for ν_{sat} that are compatible with both a particular choice of integers (l, m, p) or full filling of a meaningful unit-cell area A_{hyp}. For example, if p is small, the associated A_{hyp} becomes sufficiently large to be potentially caused by full filling of the supermoiré unit cell.

While we cannot uniquely identify the two variables p and m from a measurement of ν_{sat}, we can identify plausible candidates. Plausible in this context means that the size of the superstructure is below 50 nm × 50 nm = 2500 nm^2, such that the influence of twist-angle variations on the satellite features are less likely. Consequently, we expect small integers for the parameters l and m. Considering simple fractions that correspond to a commensurate moiré lattice and yield a ν_{sat} within the experimental error bounds (see Appendix B), one finds $(l = 13,\ p = 8)$ yielding, according to Eq. (2), $\nu_{\mathrm{sat}} = 4 \times \frac{8}{13} \approx 2.46$ (see Appendix G). To determine the corresponding value of the parameter m, we search for an area ratio yielding a commensurate supermoiré lattice, which gives $m = 16$ (see also Fig. 13 in Appendix G for a schematic illustration). Assuming these values, we can estimate the twist angle of the graphene/hBN moiré lattice by using the general geometric relation between the moiré unit-cell size $\lambda_{\mathrm{gr/hBN}} = [2A_{\mathrm{gr/hBN}}/\sqrt{3}]^{1/2} = (13.05 \pm 0.50)$ nm to calculate the twist angle via [52]

$$\theta_{\mathrm{gr/hBN}} = \arccos\left[1 - \frac{(1+\delta)a^2}{2\lambda_{\mathrm{gr/hBN}}^2} + \frac{\delta^2}{2(1+\delta)}\right], \qquad (3)$$

where $\delta \approx 0.017$ is the relative lattice constant mismatch between graphene and hBN. This results in an extracted twist angle of $\theta_{\mathrm{gr/hBN}} = 0.50^{\circ} \pm 0.10^{\circ}$ ($A_{\mathrm{gr/hBN}} \approx 147.5\ \mathrm{nm}^2$). This value must be treated with caution, as the next largest possible commensurate moiré system (just larger by a factor of about 1.3), providing ν_{sat} values within the experimental error bars, is defined by $(l = 13,\ m = 21,\ p = 8)$, giving a graphene/hBN twist angle of $\theta_{\mathrm{gr/hBN}} = 0.79^{\circ} \pm 0.08^{\circ}$ ($A_{\mathrm{gr/hBN}} \approx 112.5\ \mathrm{nm}^2$). These different estimates nicely illustrate the difficulty of determining the twist angle in such multilayer van der Waals heterostructures. In both cases, the noninteger fraction ν_{sat} of full filling of the tBLG unit cell at which we find the additional Landau fans can be expressed as a simple fraction, as predicted by Eq. (2).

Note that the requirement for the appearance of the additional Landau fans resulting from the graphene/hBN moiré lattice is commensurability. In an incommensurate supermoiré lattice, one would always select different subsets of tBLG AA sites, which does not result in a well-defined band gap. Only in the commensurate case, a sufficient number of repetitions in the resulting superstructure selects the same, well-defined subsets of tBLG AA sites within each supermoiré unit cell, imprinting a band gap on the density of states. We can investigate the minimal number of repetitions required numerically: we find that a prominent gap in the density of states only emerges upon inclusion of the order of five periodic cells in one direction. Estimating the characteristic size of the supermoiré unit cell as $\sqrt{lA_{\mathrm{gr/hBN}}} = \sqrt{13 \times 147.5}$ nm ≈44 nm results in a minimum length scale of the commensurate area of ≈220 nm, in agreement with the typical size of domains with constant twist angle as reported in Ref. [53]. We, however, expect that the commensurability also contributes to the stabilization of the moiré geometry suppressing twist-angle inhomogeneities resulting in even significantly larger domains. This reduces the disorder for the Bloch states in the graphene/hBN moiré lattice, making the additional Landau fan more prominent.

V. CONCLUSION

In conclusion, our work shows that the alignment of hBN can induce additional periodicity in tBLG-based van der Waals heterostructures. Our theoretical model shows that the resulting superstructure leads to additional band gaps and Landau fans, which we experimentally observe. We find that the graphene/hBN moiré lattice acts as an additional periodic potential that breaks the symmetry between AA sites of the tBLG moiré lattice. As a consequence, the additional Landau fans do not emerge at full filling of a unit cell of certain size, but instead at full filling of a subset of selected AA sites within the supermoiré unit cell. Thus, our work shows that the effects of moiré materials can extend to the length scales of tens of nanometers, and that the appearance of additional

Landau fans does not directly imply an associated supercell of related size. In future work, further investigation of such corresponding structures may also shed light on the formation and stabilization of correlated phases in hBN-aligned tBLG heterostructures.

The data supporting the findings of this study are available in a Zenodo repository under Ref. [54].

ACKNOWLEDGMENTS

This work was supported by the FLAG-ERA grants TATTOOS (Grant No. 437214324), PhotoTBG (Grant No. 471733165) and 2D-NEMS (Grant No. 436607160) by the Deutsche Forschungsgemeinschaft (DFG, German Research Foundation) under Germany's Excellence Strategy Cluster of Excellence Matter and Light for Quantum Computing (ML4Q) EXC 2004/1–390534769, within the Priority Program SPP 2244 "2DMP"-443273985, the Helmholtz Nano Facility [55] and by the FWF doctoral school TU-DX, Grant https://doi.org/10.55776/DOC142. K.W. and T.T. acknowledge support from the JSPS KAKENHI (Grants No. 20H00354, No. 21H05233, and No. 23H02052) and World Premier International Research Center Initiative (WPI), MEXT, Japan. C.Sc. acknowledges support as a recipient of a DOC fellowship of the Austrian Academy of Sciences. Numerical calculations were in part performed on the Vienna Scientific Cluster VSC4 and VSC5.

C.Sc. and F.Li. performed the theoretical simulations. A.R. built the device. S.T. and F.Le. performed the electron beam lithography. A.R. and R.J.D. performed the measurements and analyzed the experimental data. A.R., R.J.D., C.Sc., F.Li. and C.St. discussed the experimental and theoretical data with input from B.B. and D.M.K. K.W. and T.T. supplied the hBN crystals. A.R., C.Sc., R.J. D., D.M.K., B.B., F.Li., and C.St. wrote the manuscript.

APPENDIX A: SAMPLE FABRICATION

We start our fabrication procedure with exfoliating graphene, graphite (Naturgraphit GmbH), and hBN on standard Si/SiO_2 wafers (oxide thickness: 90 nm). Suitable flakes for the further process are identified by optical microscopy. The fabrication of the tBLG follows the "laser cut and stack" technique [56] using a polycarbonate/polydimethylsiloxane (PC/PDMS) droplet [57]. We adjust a tBLG twist angle of 1.3°, while the composite hBN/graphene moiré lattice is formed by aligning the crystallographic axes of the bottom hBN flake with the axis of the used graphene flake. We pick up the hBN flakes (thicknesses of the top and bottom hBN flakes are approximately 25 and 30 nm, respectively) at 90 °C, while the graphene pickups are performed at 40 °C. The final pickup of the graphite back gate is performed at 120 °C. The finished stack is dropped on a marked Si/SiO_2 chip at 165 °C. We remove the PC with chloroform and clean the stack with isopropanol. An optical image of the final stack is shown in Fig. 6. The graphite flake is used as a back gate, allowing homogeneous gating and screening of the potential disorder from the substrate [58]. With

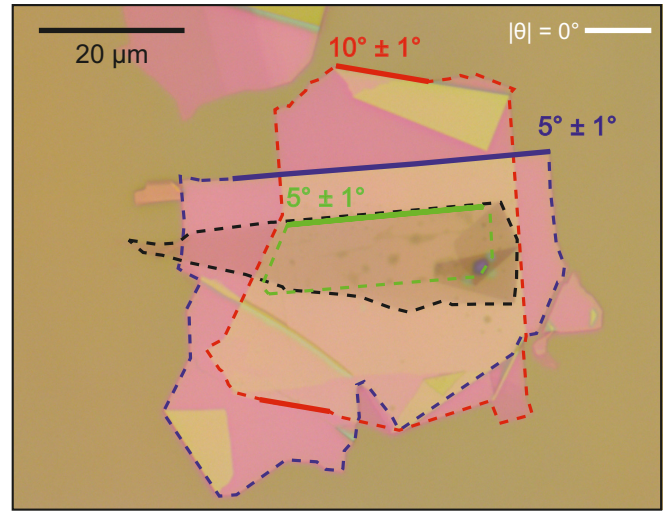

FIG. 6. Optical image of the fabricated van der Waals heterostructure. The dashed lines show the outlines of graphite (black), tBLG (green), top hBN (red), and bottom hBN (blue) flakes. The graphene/hBN moiré lattice is formed on the interface between the bottom hBN and a single-layer graphene flake. Solid lines show the crystallographic axes used for the (mis)alignment during the fabrication. The angles are given with respect to the horizontal white line.

standard electron beam lithography and reactive ion etching (CF_4/O_2) techniques we define Ohmic contacts to the tBLG [59,60] which are subsequently evaporated (Cr/Au, 5/50 nm). With a further lithography and metal evaporation step, we define the lines to the etched contacts (Cr/Au, 5/50 nm). The Hall bar geometry is defined after hard mask evaporation (Al, 60 nm) by a final reactive ion etching step (SF_6/O_2). Finally, we remove the aluminium hard mask in TMAH (2.38% in DI water).

APPENDIX B: CONVERSION TO DENSITY AXIS, TWIST-ANGLE EXTRACTIONS, AND ERROR ESTIMATIONS

To convert the applied back-gate voltage to the adjusted charge carrier density, we extract the lever arm of the graphite back gate α_{bg} from the slopes of the visible Landau levels emerging from the charge-neutrality point. The slopes are found by least-squares fitting to the minima in resistance in the magnetotransport data. The corresponding filling sequence of the Landau levels emerging from the central fan is given by $\nu_{LL} = \pm 4, \pm 8, \pm 12$. We calculate the lever arm using

$$B_{LL} = \frac{h}{\nu_{LL} e} \alpha_{bg} V_{bg} + \text{const.} \tag{B1}$$

This results in a numerical value of $\alpha_{bg} = (5.148 \pm 0.129) \times 10^{15}\ \mathrm{V^{-1} m^{-2}}$. This value is in reasonable agreement with the geometric lever arm expected from a simple plate capacitor model:

$$\alpha_{bg} = \varepsilon_0 \varepsilon_{hBN} \frac{1}{ed}, \tag{B2}$$

which yields a value of $\alpha_{bg} \approx 6.263 \times 10^{15}\ \mathrm{V^{-1}\,m^{-2}}$. Here, we used $\varepsilon_{hBN} = 3.4$ [61,62] and a thickness of $d \approx 30$ nm

for the bottom hBN flake which was extracted via atomic force microscopy. We note that we observed an extrinsic doping in our device leading to a shift of the charge-neutrality point away from $V_{bg} = 0$ V. During the data analysis we corrected for this extrinsic shift by fitting according to $n = \alpha_{bg}(V_{bg} - V_{bg,off})$ with $V_{bg,off} = 112$ mV. The uncertainty on the experimentally extracted lever arm was used to quantify the uncertainties on the extracted twist angles of the two moiré lattices.

We estimate the tBLG moiré superlattice density to be $n_s = (2.17 \pm 0.06) \times 10^{12}$ cm^{-2}, which gives a moiré unit-cell area of $A_{tBLG} = 4/n_s = (184.3 \pm 5.1)$ nm^2. Via $\theta_{tBLG} = [\sqrt{3}n_s a^2/8]^{1/2}$ this directly propagates to a tBLG twist angle of $\theta_{tBLG} = 0.97^\circ \pm 0.02^\circ$. To determine the error, we calculate the twist angle with the density values $n_s^+ = 2.23 \times 10^{12}$ cm^{-2} and $n_s^- = 2.11 \times 10^{12}$ cm^{-2} and choose the larger deviation from our mean value as the error bound (this value agrees with the result obtained from Gaussian error propagation). The additional Landau fan feature emerges at a charge carrier density of $n = (1.36 \pm 0.06) \times 10^{12}$ cm$^{-2} \equiv n_{sat}$ which corresponds on the filling factor axis to $\nu_{sat} = 4n_{sat}/n_s = 2.50 \pm 0.11$. Here again, we are estimating the uncertainty by calculating the filling factor via n_{sat}^+ and n_{sat}^- and giving the larger bound (calculation is done with the mean value of $n_s = 2.17 \times 10^{12}$ cm^{-2}). As stated in the main paper, assigning this satellite to full filling of a hypothetical moiré unit cell of size A_{hyp} would result in $A_{hyp} = 4/n_{sat} = 4A_{tBLG}/\nu_{sat} = (1.60 \pm 0.07)A_{tBLG}$. Associating this hypothetical moiré unit cell with a graphene/hBN moiré unit cell results in a moiré superlattice wavelength of $\lambda_{hyp}^{gr/hBN} = [2A_{hyp}/\sqrt{3}]^{1/2} \approx 18.5$ nm > 14.7 nm $\approx \lambda_{max}^{gr/hBN}$, which is larger than the theoretically maximal value of $\lambda_{max}^{gr/hBN}$ for a graphene/hBN moiré lattice [29]. Since $A_{hyp} < 2A_{tBLG}$ holds, the area A_{hyp} can also not correspond to any supermoiré lattice. We thus conclude that the observed satellite is caused by the discussed real-space effect, yielding to the selection rule

$$\nu_{sat}(l, p) = 4\frac{p}{l} = 4\frac{pA_{tBLG}}{mA_{gr/hBN}},$$
$$lA_{tBLG} = mA_{gr/hBN}, \qquad p < l \tag{B3}$$

where l and m are the numbers of the tBLG and graphene/hBN unit cells and p is the number of selected tBLG AA sites. The experimental observed value of ν_{sat} suggests *a priori* simple fractions like $p/l = \frac{5}{8}$, $\frac{7}{11}$, or $\frac{8}{13}$ which are all within the experimental uncertainty. In the next step, we consider the possible ratios m/l of the commensurate areas of the two moiré unit cells. The simulated ratio of $A_{tBLG}/A_{gr/hBN} = m/l = \frac{4}{3}$ implies for both possible values of $p = 1, 2$ either $\nu_{sat}(l, p) = \nu_{sat}(3, 2) \approx 2.67$, which is close to the estimated error bound, or $\nu_{sat}(l, p) = \nu_{sat}(3, 1) \approx 1.33$, which is far off. There are, however, other commensurate unit-cell structures with rations $A_{tBLG}/A_{gr/hBN} = \frac{16}{13}$ or $\frac{21}{13}$ resulting in $\nu_{sat}(l, p) = \nu_{sat}(13, 8) \approx 2.46$, which are both in line with the experimental value. In principle, the experimental value of $\nu_{sat} \approx 2.50$ implies for the ratio m/l a denominator l of, e.g., 8 ($4p/l = 4 \times \frac{5}{8} = 2.5$), 11 ($4 \times \frac{7}{11} = 2.54$), or 13 ($4 \times \frac{8}{13} = 2.46$). We note, that for $l = 8, 11$, there are no commensurate moiré superstructures with a reasonable graphene/hBN moiré unit-cell size (see Appendix G). This leaves a fraction of $A_{tBLG}/A_{gr/hBN} = m/l = \frac{16}{13}$ for the area ratio as the closest fit to the experimental result for ν_{sat}. A further culprit for the remaining differences between theory and experiment might also be limitations of our model geometry, which does not allow for additional corrugations of the tBLG due to the additional hBN/graphene moiré lattice, for shearing of the moiré unit cell that affects the symmetry of the reconstruction or relaxation effects in the tBLG/hBN heterostructure. Consequently, the simplest case $m/l = \frac{4}{3}$, slightly outside of the experimental error bars, might potentially also be relevant.

The twist angle of the graphene/hBN moiré lattice can now be estimated for different possible cases. To do this, we trace back the graphene/hBN unit-cell area to the tBLG moiré unit cell area via $A_{gr/hBN} = 4pA_{tBLG}/(m\nu_{sat})$. For the two cases ($l = 3, m = 4, p = 2$) and ($l = 13, m = 16, p = 8$) this leads to identical results (since $p/m = \backslash frac24 = \frac{8}{16}$) with a numerical value of $A_{gr/hBN} = (147.5 \pm 11.1)$ nm^2 (we estimate the uncertainty by using $A_{tBLG}^+ = 189.4$ cm^{-2} and $\nu_{gr/hBN}^- = 2.39$ to calculate $A_{gr/hBN}^+ = 158.6$ nm^2 and vice versa for $A_{gr/hBN}^- = 137.4$ nm^2; we then choose the larger deviation from the mean value to define our error bound). This result is equivalent to an area ratio of $A_{tBLG}/A_{gr/hBN} = 2\nu_{sat}/4 = 1.25 \pm 0.06$ (with $\nu_{sat} = 2.50 \pm 0.11$). Now, by exploiting $\lambda_{gr/hBN} = [2A_{gr/hBN}/\sqrt{3}]^{1/2}$ we calculate (error estimation again via $A_{gr/hBN}^{\pm}$) a numerical value of $\lambda_{gr/hBN} = (13.05 \pm 0.50)$ nm, which results finally via [52]

$$\theta_{gr/hBN} = \arccos\left[1 - \frac{(1+\delta)a^2}{2\lambda_{gr/hBN}^2} + \frac{\delta^2}{2(1+\delta)}\right] \tag{B4}$$

in a graphene/hBN twist angle of $\theta_{gr/hBN} = 0.50^\circ \pm 0.10^\circ$ (again estimated by performing the calculation with $\lambda_{gr/hBN}^{\pm}$). The third case discussed in the main paper ($l = 13, m = 21, p = 8$) yields in analogous calculation for the graphene/hBN moiré unit-cell area a value of $A_{gr/hBN} = (112.4 \pm 8.5)$ nm^2 (area ratio $A_{tBLG}/A_{gr/hBN} = 1.64 \pm 0.07$), corresponding to a moiré superlattice wavelength of $\lambda_{gr/hBN} = (11.39 \pm 0.44)$ nm. This results in a corresponding twist angle of $\theta_{gr/hBN} = 0.79^\circ \pm 0.08^\circ$. Further possible commensurate cases up to ($l = 13, m = 25$) are listed in Table I in Appendix G.

APPENDIX C: INITIAL CHARACTERIZATION OF THE DEVICE

The experiments are performed in a ^{3}He/^{4}He dilution refrigerator at a base temperature of around 30 mK using standard DC and low-frequency lock-in measurement techniques. We initially characterize our device by temperature-dependent transport measurements. An atomic force microscopy image of the sample is shown in Fig. 7(a), while Fig. 7(b) shows a cross section of the van der Waals heterostructure. To verify the existence of a tBLG moiré lattice, we start characterizing our device by measuring the two-terminal differential conductance dI/dV_{2T} as a function of the charge carrier density n adjusted by the graphite back-gate voltage by applying a symmetric AC bias of $V_{AC} = 100$ μV along the entire Hall bar structure [see Fig. 7(a)] and separately measuring the

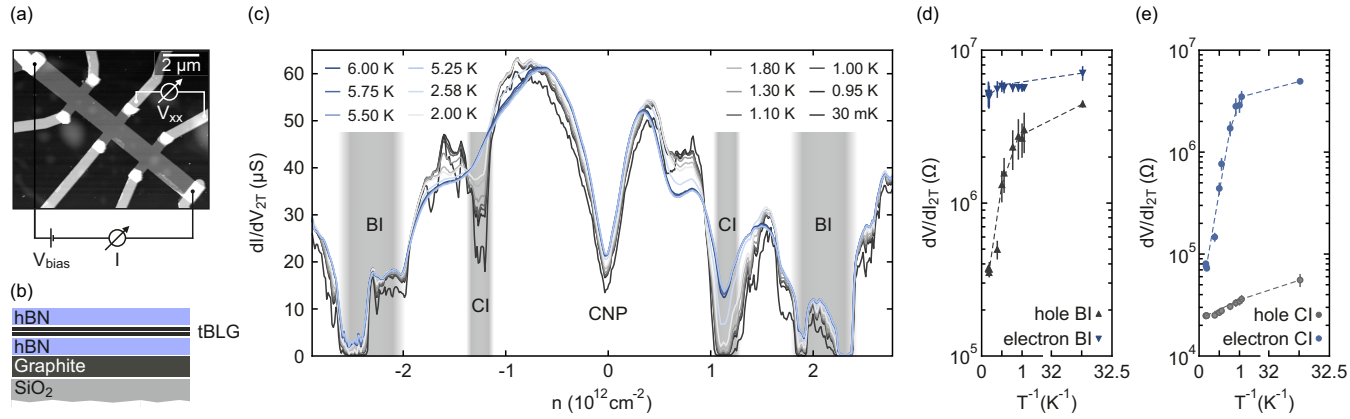

FIG. 7. (a) Atomic force microscopy image of the measured device. The electrical connections for the two- and four-terminal measurements are depicted. (b) Schematic cross section of the device showing the composition of the heterostructure. (c) Two-terminal differential conductance dI/dV_{2T} as a function of the charge carrier density n for different temperatures measured along the entire Hall bar structure. The minima in conductance correspond to the band insulators (BI), correlated insulators (CI), and the charge-neutrality point (CNP) (d) Arrhenius plot of the differential resistance dV/dI_{2T} of the band-insulating states as a function of the inverse temperature. The individual data points are extracted by taking the mean of the minima in the band-insulating states. The error bars represent the standard deviations. (e) Same as in (d), but for the correlated-insulating states.

current via an in-house built IV converter (gain: 10^7 VA^{-1}) for different temperatures T [see Fig. 7(c)]. With decreasing temperature we observe multiple dips in differential conductance at certain charge carrier densities, which can be assigned to both, correlated-insulating states (CI) and band-insulating states (BI) [10,11,13]. From the rapid decrease of differential conductance as a function of temperature, we identify the insulating features around $n_s/2 \approx \pm 1.085 \times 10^{12}$ cm^{-2} as correlated-insulating states [see also the Arrhenius plot in Fig. 7(e)]. Here, n_s denotes the superlattice density, i.e., the density which we associate with the edges of the flat bands. Consequently, the dips in differential conductance around $n_s \approx \pm 2.17 \times 10^{12}$ cm^{-2} correspond to the band-insulating states (BI) or full filling of four holes or electrons of the tBLG moiré superlattice unit cell while the correlated-insulating states at $n \approx \pm 1.085 \times 10^{12}$ cm^{-2} correspond to half-filling of two holes or electrons of the tBLG moiré superlattice unit cell [see Fig. 7(c) and the Arrhenius plot in Fig. 7(d)]. The hole-doped band insulator shows a plateau in differential conductance emerging at a charge carrier density of $n \approx -2 \times 10^{12}$ cm^{-2} until the minimum is reached at $n \approx -2.4 \times 10^{12}$ cm^{-2}. Likewise, the band insulator at electron doping appears to be split in two separate insulating features around charge carrier densities of $n \approx 1.95 \times 10^{12}$ cm^{-2} and $n \approx 2.3 \times 10^{12}$ cm^{-2}.

We attribute this distorted shape to twist-angle variations along our device [53,63,64], preventing a clean gap opening [65]. This interpretation is supported by the comparison of two- and four-terminal magnetotransport data in Fig. 8 where the splitting of the electron-doped band insulator is only visible for the two-terminal measurement and additional finite-bias spectroscopy measurements on the band-insulating states [see Figs. 9(a) and 9(b)]. The temperature-activated transport data of the band-insulating gaps [Fig. 7(d)] show a qualitative asymmetry between the hole- and electron-doped sites. Over the accessible temperature range, the hole-doped band insulator shows a clear thermal activation while the corresponding band insulator at electron doping is barely affected up to the maximum temperature of $T = 6$ K. This asymmetry is indicative of a difference in the size of the energy gap between electron and hole sides, in accordance with the band structure calculations shown in Fig. 2 (see also Fig. 12).

TABLE I. Supermoiré unit cells for tBLG and graphene/hBN submoiré lattices with comparatively small areas, l is the number of tBLG moiré unit cells, m the number of graphene/hBN unit cells, and p the number of selected AA sites in the supermoiré unit cell. The column A_{sm} refers to the total area of the supermoiré unit cell. [For the case ($l = 12, m = 13, p = 8$), the superlattice wavelength of the graphene/hBN moiré lattice yields a numerical value of $\lambda_{gr/hBN} = (14.47 \pm 0.55)$ nm. The upper bound is thus larger than theoretically possible for a graphene/hBN moiré lattice.]

l	m	p	A_{sm} (nm^2)	$\nu_{gr/hBN} = 4p/l$	$\theta_{gr/hBN}$ (deg)	φ (deg)
3	4	2	530	2.67	0.50 ± 0.10	90
4	7	3	706	3	0.67 ± 0.08	100
7	9	4	1236	2.28	0.63 ± 0.09	100
9	13	6	1589	2.67	0.59 ± 0.09	73
9	16	6	1589	2.67	0.81 ± 0.08	60
12	13	8	2119	2.67	0.18 ± 0.15	76
12	19	8	2119	2.67	0.69 ± 0.08	76
13	16	8	2296	2.46	0.50 ± 0.10	106
13	19	8	2296	2.46	0.69 ± 0.08	82
13	21	8	2296	2.46	0.79 ± 0.08	95
13	25	8	2296	2.46	0.96 ± 0.08	106

APPENDIX D: INFLUENCE OF TWIST-ANGLE DISORDER

Twist-angle variations along the device are visible in magnetic field- and bias-dependent measurements. In Fig. 8 we compare the two-terminal differential resistance measured as a function of magnetic field and carrier density along the entire Hall bar structure [Fig. 8(a)] and the corresponding

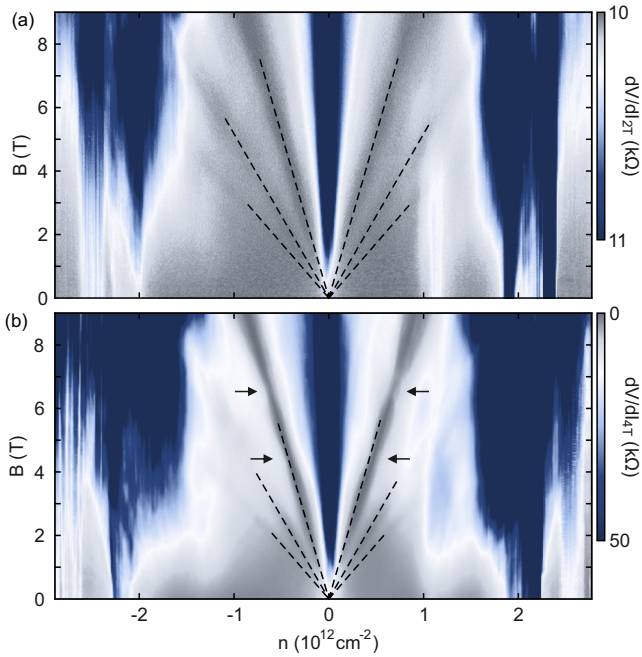

FIG. 8. (a) Two-terminal differential resistance as a function of magnetic field and carrier density measured along the entire Hall bar structure [compare with Fig. 7(a)]. (b) Four-terminal differential resistance measured in the configuration shown in Fig. 7(a) as a function of magnetic field and carrier density. The black arrows mark the positions where the Landau levels emerging from the graphene/hBN moiré lattice intersect with the Landau levels emerging from the tBLG moiré lattice. Visible is the narrowing of the lowest Landau level emerging from the charge-neutrality point at the certain intersection positions.

four-terminal measurement of the longitudinal resistance [Fig. 8(b)]. The splitting of the electron-doped band insulator around $n \approx 2 \times 10^{12}$ cm^{-2} is absent in the four-terminal measurement indicating that it is caused by twist-angle variations along the device. Furthermore, in the four-terminal data, narrowing features are present in the most prominent Landau level emerging from the charge-neutrality point (see black arrows). These features correspond to the intersection points between the fan emerging from charge neutrality and the additional hBN-induced Landau fan. Therefore, they might indicate the presence of Bloch states (Brown-Zak fermions) caused by restoring the translational symmetry in the graphene/hBN moiré lattice. Note that the indications of a graphene/hBN moiré lattice are only visible in the four-terminal data which might be explained with a rather homogeneous twist-angle distribution in that particular area of the device. In Figs. 9(a) and 9(b) we show two-terminal finite-bias spectroscopy measurements of the band-insulating (BI) states. We do not observe a single diamond-shaped feature of suppressed differential conductance but instead the formation of a multitude of individual Coulomb diamonds which are most prominent in the hole regime. We attribute this to the formation of different moiré domains in the tBLG superlattice with slightly different twist angles as sketched in Fig. 9(c). The electron-doped BI seems to be slightly less affected from the twist-angle disorder. This might be due to stronger stability of this gap compared to the hole-doped BI, which was also observed in the temperature dependence. This is noticeable in higher-bias values which are necessary to break through the gap. The difference in the bias values necessary to break through the gaps for both dopings also indicates the mentioned asymmetry visible in the band structure calculation.

APPENDIX E: MODELING TWO MOIRÉ LATTICES IN UNISON

We combine an atomistic tight-binding Hamiltonian parametrized from DFT calculations with a continuum elasticity model that accounts for lattice relaxation in tBLG with an effective symmetry-breaking potential that accurately captures the influence of alignment to an hBN layer. The local stacking configuration of the two rotated graphene layers (parametrized via a displacement vector $\vec{d}$) changes throughout the large moiré super cell (Fig. 10). We sample the two-dimensional configuration space of the displacement vector $\vec{d}$ with a 10×10 grid of DFT calculations for periodic, primitive-cell calculations mapping the configuration space of different displacements $\vec{d}$ [Fig. 10(b)]. We obtain tight-binding parameters for intermediate stackings using Fourier interpolation. We can then map the different local stackings within the large supercell to the corresponding tight-binding parameters. For the primitive bilayer DFT calculations, we use VASP [66] with LDA, 25×25 Monkhorst $\vec{k}$-space grid, and a plane-wave cutoff of 380 eV. Atomic positions are relaxed in out-of-plane direction but fixed in plane. We then project all Kohn-Sham orbitals onto one p_z orbital per carbon site (via WANNIER90 [67–69]) and thus capture all the influence of the tBLG moiré lattice that is relevant for electronic transport close to the Fermi energy. From this point on we can smoothly interpolate tight-binding couplings γ_{ij} across the entire moiré supercell. However, we have yet to account for the significant strain fields of the real moiré supercell. We do so via exponential correction factors that depend on the local strain:

$$\gamma_{i,j}^{(\mathrm{corr})} = \gamma_{i,j} \mathrm{e}^{-\Delta l_{ij} \alpha_{ij}}, \tag{E1}$$

where Δl_{ij} is the change in interorbital distance due to mechanical relaxation and α_{ij} encodes the distance sensitivity of individual tight-binding hopping parameters. We determine the α_{ij} from a set of DFT calculations on primitive unit cells of strained single-layer graphene with subsequent Wannierization. Finally, we determine the Δl_{ij} via an approach that resembles the elasticity models of Nam and Koshino [41]. Such an approach determines an equilibrium configuration that balances energy gain due to more favorable stacking fault energies with the elastic energy cost associated with in-plane displacements. The corresponding energy functional is of the form

$$U_{\mathrm{tot}} = U_{\mathrm{E}}[\vec{u}_{\mathrm{bot}}] + U_{\mathrm{E}}[\vec{u}_{\mathrm{top}}] + U_{\mathrm{B}}[\vec{u}_{\mathrm{bot}}, \vec{u}_{\mathrm{top}}], \tag{E2}$$

where $\vec{u}_{\mathrm{bot/top}}$ are the local displacement vectors in bottom and top layer, respectively. The third, stacking-dependent term is elegantly expressed via the first few Fourier components $c_{\vec{G}}$ of the generalized stacking fault energy:

$$U_{\mathrm{B}}[\vec{u}_{\mathrm{bot}}, \vec{u}_{\mathrm{top}}] = \int \sum_{\vec{G}} c_{\vec{G}} \mathrm{e}^{\mathrm{i}((\vec{d}+\vec{u}_{\mathrm{bot}}-\vec{u}_{\mathrm{top}})\cdot\vec{G})} \mathrm{d}\vec{r} \tag{E3}$$

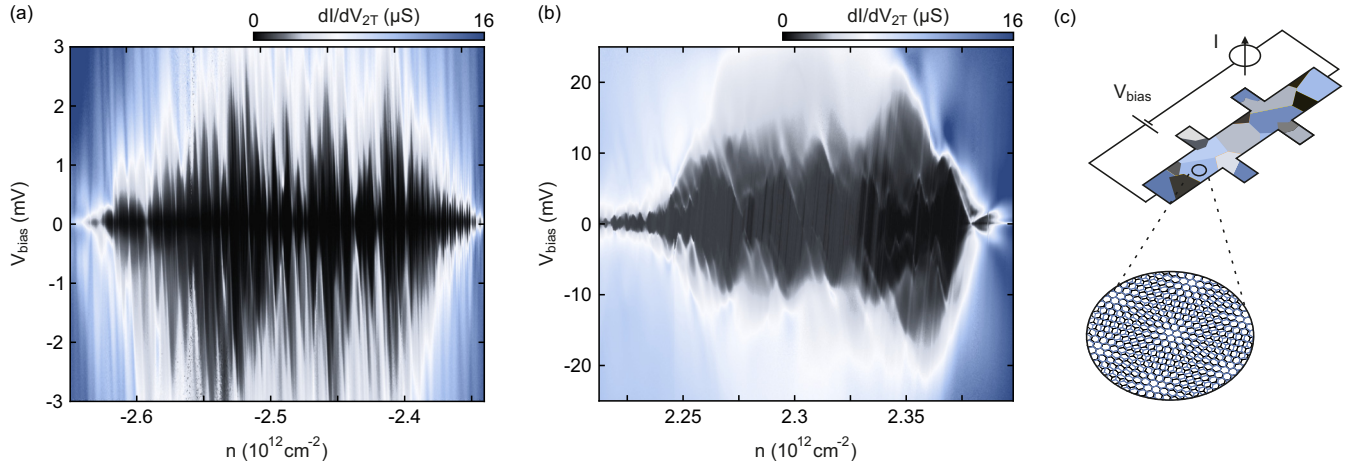

FIG. 9. (a) Finite-bias spectroscopy on the hole-doped BI state showing individual Coulomb diamonds. (b) Same as in (a) but for the electron-doped BI. (c) Schematic illustration of the measurement setup.

with $\vec{G}$ running over reciprocal lattice vectors. The intralayer contributions U_{E} of both layers (m = top/bot) read as

$$U_{\mathrm{E}}[\vec{u}^{\mathrm{m}}] = \int \left[\frac{\lambda+\mu}{2} \left(\frac{\partial u_x^{\mathrm{m}}}{\partial x} + \frac{\partial u_y^{\mathrm{m}}}{\partial y} \right)^2 + \frac{\mu}{2} \left(\left(\frac{\partial u_x^{\mathrm{m}}}{\partial x} - \frac{\partial u_y^{\mathrm{m}}}{\partial y} \right)^2 + \left(\frac{\partial u_x^{\mathrm{m}}}{\partial y} + \frac{\partial u_y^{\mathrm{m}}}{\partial x} \right)^2 \right) \right] \mathrm{d}\vec{r} \tag{E4}$$

with Lamé parameters $\lambda = 3.25\ \mathrm{eV\,Å^{-2}}$ and $\mu = 9.57\ \mathrm{eV\,Å^{-2}}$. We then solve the Euler-Lagrange equations of the system following closely along the procedures in [41].

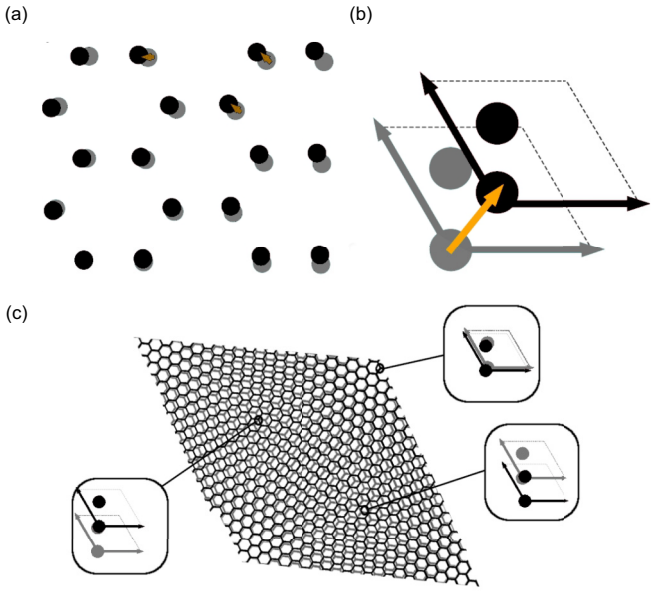

FIG. 10. (a) Closeup of twisted bilayer graphene (large angle for clarity) (black: top layer, gray: bottom layer). (b) Unit cell in the x-y plane with local displacement vector $\vec{d}$. (c) Unit cell of tBLG. Each local configuration can be mapped to a unit cell (see insets) with a corresponding shift.

The main result of this relaxation is the proliferation of the energetically favorable AB stacking region in the upper left half of the moiré supercell.

We next consider models for the additional second moiré lattice between hBN and one graphene sheet of the tBLG. Due to the wide band gap of hBN, there is no need to explicitly model the nitrogen and boron atoms themselves. Instead, we use additional onsite corrections of the p_z orbitals of the graphene sheet. We describe the effect of the hBN via a slowly varying background potential V_i and a short-range symmetry-breaking potential W_i [43]:

$$V_{\mathrm{hBN}} = \sum_{i=\mathrm{I,III,V}} V_i \mathrm{e}^{-\frac{(\mathbf{r}-\mathbf{R}_i)^2}{2w_i^2}} \sigma_0 \otimes \tau_0 + \sum_{i=\mathrm{I,III,V}} W_i \mathrm{e}^{-\frac{(\mathbf{r}-\mathbf{R}_i)^2}{2w_i^2}} \sigma_z \otimes \tau_0, \tag{E5}$$

where w_i are characteristic length scales, σ_0 (σ_z) represent unity (z-Pauli matrix) in sublattice space, and τ_0 is the unity in valley space. The W_i terms proportional to σ_z reflect the short-range variations in local chemical environment between adjacent carbon atoms (e.g., in a configuration where one carbon atom sits on top of a nitrogen and the other on a boron atom. While the V_i break particle-hole symmetry, the W_i introduce sublattice asymmetry. Derived from DFT calculations [44,45] these terms can accurately describe the effect of hBN alignment with respect to one of the graphene layers. We partition the graphene/hBN moiré unit cell in five regions based on relative local alignment with the graphene layer (see Fig. 11). Assigning different amplitudes ($V_{\mathrm{I}} = V_{\mathrm{III}} = 0$ meV, $V_{\mathrm{V}} = 100$ meV, $W_{\mathrm{I}} = 57$ meV, $W_{\mathrm{III}} = -34$ meV, $W_{\mathrm{V}} = -47$ meV) and widths ($0.63 w_{\mathrm{I}} = w_{\mathrm{III}} = w_{\mathrm{V}} = 7$ nm) to the Gaussians in Eq. (E5) allows us to effectively model the influence of the hBN alignment and introduces the second moiré lattice length scale into the tBLG Hamiltonian in an elegant and easily adaptable manner. This adaptability is very important for us to create structures with feasible periodicity. The relaxed displacement-mapping method we use for the derivation of the tBLG tight-binding Hamiltonian can only be applied to commensurate twist angles θ_{tBLG}.

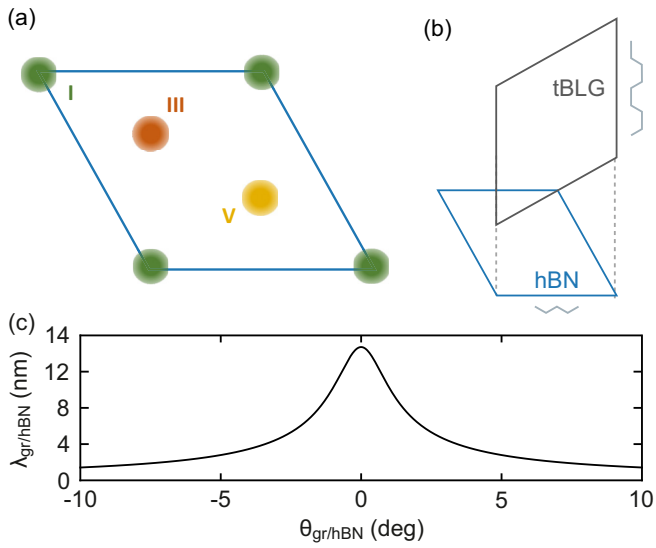

FIG. 11. (a) Schematic of the real-space moiré superlattice unit cell of the graphene/hBN system. Colored circles (I,II,V) correspond to centers of Gaussians used in the effective moiré potential. (b) Schematic explanation of the superposition of the two moiré lattices. Light gray lines indicate edge character of the unit cells. Assuming a small graphene/hBN twist angle of $\theta_{\mathrm{gr/hBN}} \approx 0.62^\circ$ brings the two moiré cells to the same periodicity. (c) Lattice constant of the graphene/hBN moiré lattice as a function of their relative twist angle $\theta_{\mathrm{gr/hBN}}$.

Having access to a set of different twist angles of tBLG Hamiltonians we identify $\theta_{\mathrm{tBLG}} = 0.987^\circ$ as the closest one to the experimentally determined twist angles. The unit cell for this moiré system is spanned by the vectors $\mathbf{a}_1 = (14.3, 0)^T$ nm and $\mathbf{a}_2 = (-7.1, 12.4)^T$ nm and features armchair borders. The effective hBN potential is derived for a perfectly aligned graphene/hBN moiré cell [$\mathbf{b}_1 = (13.8, 0)^T$ nm, $\mathbf{b}_2 = (-6.9, 11.9)^T$ nm] that features zigzag borders. Their difference in border character is easily reconciled via a rotation. However, this would result in a slightly different periodicity in the x direction. We avoid cumbersome duplication to their least common multiple and instead assume a slight rotation of the graphene/hBN moiré lattice. This bilayer of materials with unequal lattice constants also features an angle dependence [70] [see Fig. 11(c)]:

$$\lambda_{\mathrm{gr/hBN}} = \frac{(1+\delta)a}{\sqrt{\delta^2 + 2(1+\delta)(1-\cos\theta_{\mathrm{gr/hBN}})}}, \tag{E6}$$

where δ is the relative mismatch of lattice constants. A small twist angle $\theta_{\mathrm{gr/hBN}} = 0.62^\circ$ results in perfect agreement of x periodicity for the composite moiré system which we can then duplicate in the y direction to describe ribbons of realistic width. Terminating the edges with σ_z potentials in sublattice space suppresses surface states.

APPENDIX F: BAND STRUCTURE AND TRANSPORT CALCULATIONS

We efficiently calculate the band structure of a ribbon of several of the (by themselves already quite sizable) moiré unit cells with methods we developed in the study of graphene/hBN moiré lattices [40]. We partition the final entire tight-binding Hamiltonian into the (small) part defining the periodic boundary conditions in the x direction, H_I, and the rest, H_0. Bloch states of our structure thus follow

$$[H_0 + e^{ik\Delta x}H_I + e^{-ik\Delta x}H_I^\dagger]\psi_n = E_n\psi_n. \tag{F1}$$

To solve this equation, we employ iterative methods for the eigenvalues close to charge neutrality. We solve via shift-and-invert in combination with the Lanczos method [71]. In order to partially avoid cubic scaling we perform several independent matrix factorizations around different energies to eventually cover the range $E \in [-0.25\ \mathrm{eV}, 0.25\ \mathrm{eV}]$. The accuracy of subsequent evaluations of the conductivity depends on the sampling resolution in reciprocal space (no further improvements noticeable beyond $N_{\mathrm{kpt}} > 3000$ in our system). We optimize sampling at such high **k**-point densities by exploiting the continuity of bands along small distances in **k** space. To this extent we avoid solving the Bloch eigenvalue problem at most of the N_{kpt} **k** points and instead span a Krylov space for a subset N_{pillars} of "pillar" **k** points. Combining the Krylov spaces of two adjacent pillar points k_j and k_{j+1} generates a basis $\{b_i\}$ on which to project for all intermediate **k** points k' ($k_j < k' < k_{j+1}$) and thus evaluate band energies. The main caveat of this approach is the emergence of unphysical eigenvalues due to the artificially enlarged size of the combined Krylov spaces. We remedy this by evaluating an error norm which sees the solutions projected onto a fixed set of randomly chosen vectors $\phi_i \in \mathbb{C}^N$. This error measure vanishes for an eigenstate of the full problem and thus allows filtering out unphysical solutions. Matrix vector operations between the ϕ_i and H_0 or H_I do not depend on **k** and thus need only be evaluated once. In Fig. 12 we show the evolution of the band structure for the nonaligned (left subpanels) and aligned (right subpanels) cases with increasing tBLG twist angle.

To express the group velocity v_n, we derive Eq. (F1) with respect to k and form an expectation value

$$v_n = \frac{1}{\hbar}\frac{\partial E}{\partial k} = \frac{\mathrm{i}\Delta x}{\hbar}\phi_n^\dagger[e^{ik\Delta x}H_I - e^{-ik\Delta x}H_I^\dagger]\phi_n. \tag{F2}$$

To calculate the magnetoconductance, we include a magnetic field via Peierl's substitution. For an infinite ribbon, the conductance is simply given by the number of open modes $M_+(E)$ in positive x direction times the conductance of each mode e^2/h:

$$G(E) = \frac{e^2}{h}M_+(E). \tag{F3}$$

To approximate $M_+(E)$, we consider the integrated density of states of Bloch eigenstates moving in a single direction in a certain energy interval ΔE,

$$\rho_+(E) = \sum_{\substack{n:\, v_n(E)>0 \\ E_n<E}} 1. \tag{F4}$$

$\rho_+(E)$ is related to $M_+(E)$ via

$$M_+(E) = \frac{\rho_+(E+\Delta E) - \rho_+(E)}{\Delta E}\Delta E \approx \frac{\partial \rho_+(E)}{\partial E}\Delta E$$

for a small interval ΔE. When numerically evaluating Bloch eigenstates, one typically evaluates eigenenergies by solving

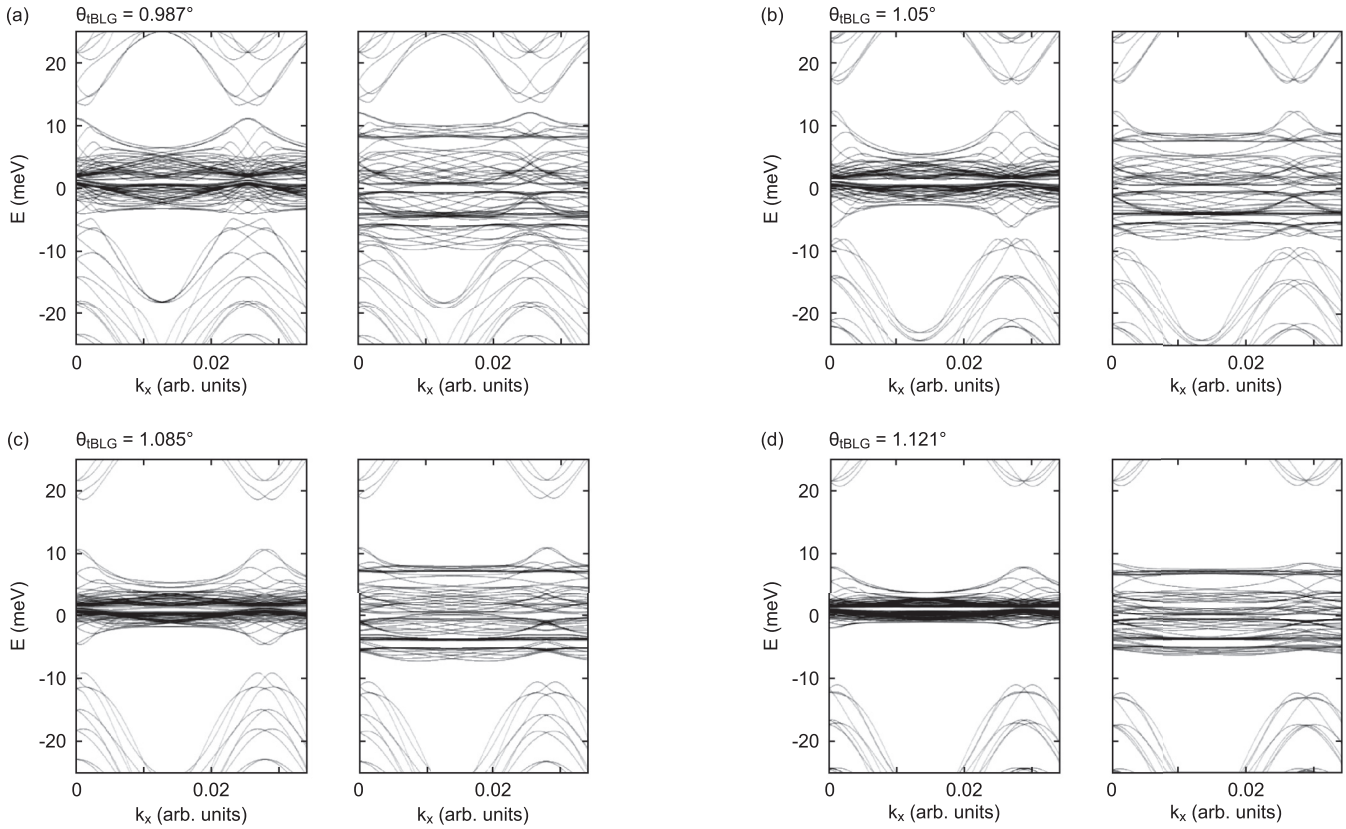

FIG. 12. Band structure calculations for different twist angles without (left subpanels) and with (right subpanels) hBN alignment.

Bloch's equation (F1) on an equidistant k grid. It is therefore convenient to replace

$$\Delta E \approx \frac{\partial E_n}{\partial k}\Delta k = \hbar v_n \Delta k.$$

Inserting these equations into (F3) yields an estimate for the conductance $G(E)$ [40]:

$$G(E) \approx \frac{e^2}{h}\frac{\mathrm{d}}{\mathrm{d}E}\sum_{\substack{n:\, v_n(E)>0 \\ E_n<E}} \hbar v_n(E)\,\Delta k. \tag{F5}$$

The use of Eq. (F5) greatly reduces the computational cost compared to calculation of $G(E)$ using the Landau-Büttiker formalism while yielding nearly identical results [40]. As our simulation contains the full information on the band structure, the energy axis can be readily transformed into the charge carrier density simply by integrating the density of states,

$$n(E) = \int_0^E \rho(E')\,\mathrm{d}E',$$

obtained from counting the bands with appropriate weight based on their group velocity. We set $n = 0$ at the charge-neutrality point $E = 0$ of graphene and express n in units of $n_0 = 1/S$, the density of one electron per tBLG moiré unit cell. Likewise, the magnetic field strength B is conveniently expressed in units of magnetic flux quanta through one moiré supercell Φ/Φ_0.

APPENDIX G: COMMENSURATE MOIRÉ STRUCTURES

We list the plausible commensurate supermoiré structures for a tBLG moiré lattice aligned with a graphene/hBN moiré lattice in Table I. As stated in the main paper, plausible in this context means that the size of the superstructure is below $50\ \mathrm{nm} \times 50\ \mathrm{nm} = 2500\ \mathrm{nm}^2$; otherwise, twist-angle inhomogeneities will probably smear out satellite features. The size of the tBLG moiré lattice is fixed by the corresponding twist angle of $\theta_{\mathrm{tBLG}} = 0.987°$. While we do not know the relative angle between the graphene layer and the adjacent hBN, it should be close to zero, otherwise the graphene/hBN moiré lattice becomes too small. We search for commensurate supermoiré unit cells (Table I) by rotating the tBLG moiré lattice and the graphene/hBN moiré lattice against each other while varying the graphene/hBN twist angle $\theta_{\mathrm{gr/hBN}}$ and thus its size. Given the two subtly different origins of the two moiré effects (different unit-cell size for graphene/hBN, twist between identical lattices for tBLG), the two moiré lattices are naturally rotated by $\varphi \approx 90°$ against each other. Large deviations from $\varphi = 90°$, up to the sixfold symmetry of the tBLG moiré lattice (φ is only defined up to 60°), do not correspond to physically realizable structures, as one graphene layer is included in both moiré structures. However, considering reconstructions due to strain, twist-angle modulations and the small moiré twist angles, φ may vary slightly around this value.

The listing in Table I contains all commensurate moiré structures with $l < 15$ and $m < 2l$. We exclude values $m >$

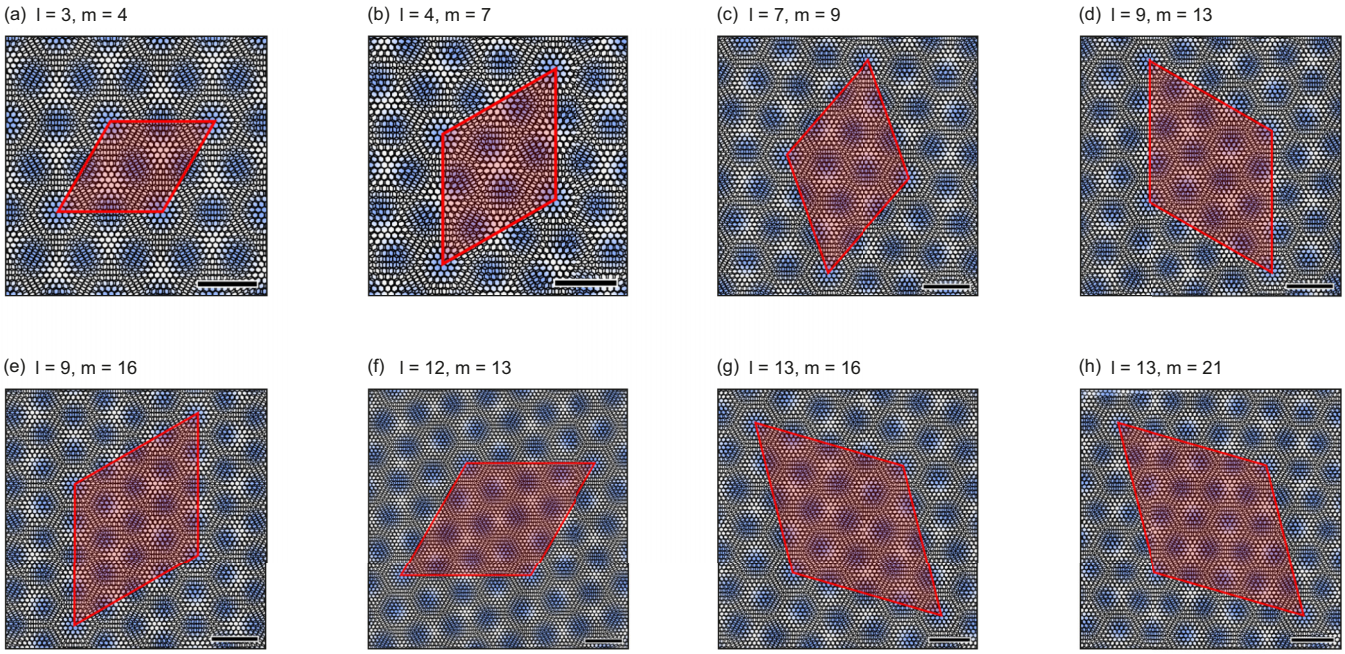

FIG. 13. Selection of commensurate moiré structures listed in Table I. Shown is the tBLG moiré lattice (black) as well as the AA site of the graphene/hBN moiré lattice (blue dots). Depending on the choice of l and m we receive a commensurate structure for different orientations φ of the two moiré lattices with respect to each other. The unit cell of the resulting supermoiré lattice is depicted as a red rhombus. The black scale bar corresponds to the spacing of the tBLG AA sites.

$2l$ as the resulting twist angles become larger, $\theta_{\mathrm{gr/hBN}} > 1^\circ$, leading to a short-ranged and quite weak moiré potential. Furthermore, we exclude larger values of l since in the presence of twist-angle disorder, larger supermoiré lattice sizes should strongly suppress the visibility of moiré satellite peaks.

Determining possible filling sequences and values of p purely based on geometry quickly becomes challenging for the larger moiré lattices, as the number of AA sites with slightly different symmetries increases. For example, the $l/m = \frac{9}{16}$ supermoiré lattice in Fig. 13 features one AA site aligned with a graphene/hBN AA site, two tBLG AA sites situated closely to an hBN site, and six tBLG AA sites at the center of three graphene/hBN AA sites. Their relative degeneracies will depend on details of the two moiré lattice potentials.

[1] F. Bloch, Über die Quantenmechanik der Elektronen in Kristallgittern, Z. Phys. **52**, 555 (1929).
[2] M. R. Slot, T. S. Gardenier, P. H. Jacobse, G. C. P. van Miert, S. N. Kempkes, S. J. M. Zevenhuizen, C. M. Smith, D. Vanmaekelbergh, and I. Swart, Experimental realization and characterization of an electronic Lieb lattice, Nat. Phys. **13**, 672 (2017).
[3] R. Drost, T. Ojanen, A. Harju, and P. Liljeroth, Topological states in engineered atomic lattices, Nat. Phys. **13**, 668 (2017).
[4] J. Figgins, L. S. Mattos, W. Mar, Y.-T. Chen, H. C. Manoharan, and D. K. Morr, Quantum engineered Kondo lattices, Nat. Commun. **10**, 5588 (2019).
[5] A. A. Khajetoorians, D. Wegner, A. F. Otte, and I. Swart, Creating designer quantum states of matter atom-by-atom, Nat. Rev. Phys. **1**, 703 (2019).
[6] C. Lagoin, S. Suffit, K. Baldwin, L. Pfeiffer, and F. Dubin, Dual-density waves with neutral and charged dipolar excitons of GaAs bilayers, Nat. Mater. **22**, 170 (2023).
[7] D. Q. Wang, Z. Krix, O. P. Sushkov, I. Farrer, D. A. Ritchie, A. R. Hamilton, and O. Klochan, Formation of artificial Fermi surfaces with a triangular superlattice on a conventional two-dimensional electron gas, Nano Lett. **23**, 1705 (2023).
[8] D. M. Kennes, M. Claassen, L. Xian, A. Georges, A. J. Millis, J. Hone, C. R. Dean, D. N. Basov, A. N. Pasupathy, and A. Rubio, Moiré heterostructures as a condensed-matter quantum simulator, Nat. Phys. **17**, 155 (2021).
[9] Y. Cao, J. Y. Luo, V. Fatemi, S. Fang, J. D. Sanchez-Yamagishi, K. Watanabe, T. Taniguchi, E. Kaxiras, and P. Jarillo-Herrero, Superlattice-induced insulating states and valley-protected orbits in twisted bilayer graphene, Phys. Rev. Lett. **117**, 116804 (2016).
[10] Y. Cao, V. Fatemi, S. Fang, K. Watanabe, T. Taniguchi, E. Kaxiras, and P. Jarillo-Herrero, Unconventional superconductivity in magic-angle graphene superlattices, Nature (London) **556**, 43 (2018).
[11] Y. Cao, V. Fatemi, A. Demir, S. Fang, S. L. Tomarken, J. Y. Luo, J. D. Sanchez-Yamagishi, K. Watanabe, T. Taniguchi, E. Kaxiras, R. C. Ashoori, and P. Jarillo-Herrero, Correlated insulator behaviour at half-filling in magic-angle graphene superlattices, Nature (London) **556**, 80 (2018).
[12] M. Yankowitz, S. Chen, H. Polshyn, Y. Zhang, K. Watanabe, T. Taniguchi, D. Graf, A. F. Young, and C. R. Dean, Tuning superconductivity in twisted bilayer graphene, Science **363**, 1059 (2019).

[13] X. Lu, P. Stepanov, W. Yang, M. Xie, M. i. Aamir, I. Das, C. Urgell, K. Watanabe, T. Taniguchi, G. Zhang, A. Bachtold, A. H. MacDonald, and D. K. Efetov, Superconductors, orbital magnets and correlated states in magic-angle bilayer graphene, Nature (London) **574**, 653 (2019).

[14] P. Stepanov, I. Das, X. Lu, A. Fahimniya, K. Watanabe, T. Taniguchi, F. H. L. Koppens, J. Lischner, L. Levitov, and D. K. Efetov, Untying the insulating and superconducting orders in magic-angle graphene, Nature (London) **583**, 375 (2020).

[15] Y. Saito, J. Ge, K. Watanabe, T. Taniguchi, and A. F. Young, Independent superconductors and correlated insulators in twisted bilayer graphene, Nat. Phys. **16**, 926 (2020).

[16] U. Zondiner, A. Rozen, D. Rodan-Legrain, Y. Cao, R. Queiroz, T. Taniguchi, K. Watanabe, Y. Oreg, F. von Oppen, A. Stern, E. Berg, P. Jarillo-Herrero, and S. Ilani, Cascade of phase transitions and Dirac revivals in magic-angle graphene, Nature (London) **582**, 203 (2020).

[17] D. Wong, K. P. Nuckolls, M. Oh, B. Lian, Y. Xie, S. Jeon, K. Watanabe, T. Taniguchi, B. A. Bernevig, and A. Yazdani, Cascade of electronic transitions in magic-angle twisted bilayer graphene, Nature (London) **582**, 198 (2020).

[18] A. L. Sharpe, E. J. Fox, A. W. Barnard, J. Finney, K. Watanabe, T. Taniguchi, M. A. Kastner, and D. Goldhaber-Gordon, Emergent ferromagnetism near three-quarters filling in twisted bilayer graphene, Science **365**, 605 (2019).

[19] M. Serlin, C. L. Tschirhart, H. Polshyn, Y. Zhang, J. Zhu, K. Watanabe, T. Taniguchi, L. Balents, and A. F. Young, Intrinsic quantized anomalous Hall effect in a moiré heterostructure, Science **367**, 900 (2020).

[20] Y. Saito, J. Ge, L. Rademaker, K. Watanabe, T. Taniguchi, D. A. Abanin, and A. F. Young, Hofstadter subband ferromagnetism and symmetry-broken Chern insulators in twisted bilayer graphene, Nat. Phys. **17**, 478 (2021).

[21] M. Oh, K. P. Nuckolls, D. Wong, R. L. Lee, X. Liu, K. Watanabe, T. Taniguchi, and A. Yazdani, Evidence for unconventional superconductivity in twisted bilayer graphene, Nature (London) **600**, 240 (2021).

[22] D. R. Klein, L.-Q. Xia, D. MacNeill, K. Watanabe, T. Taniguchi, and P. Jarillo-Herrero, Electrical switching of a bistable moiré superconductor, Nat. Nanotechnol. **18**, 331 (2023).

[23] L. A. Ponomarenko, R. V. Gorbachev, G. L. Yu, D. C. Elias, R. Jalil, A. A. Patel, A. Mishchenko, A. S. Mayorov, C. R. Woods, J. R. Wallbank, M. Mucha-Kruczynski, B. A. Piot, M. Potemski, I. V. Grigorieva, K. S. Novoselov, F. Guinea, V. I. Fal'ko, and A. K. Geim, Cloning of Dirac fermions in graphene superlattices, Nature (London) **497**, 594 (2013).

[24] J. Barrier, P. Kumaravadivel, R. Krishna Kumar, L. A. Ponomarenko, N. Xin, M. Holwill, C. Mullan, M. Kim, R. V. Gorbachev, M. D. Thompson, J. R. Prance, T. Taniguchi, K. Watanabe, I. V. Grigorieva, K. S. Novoselov, A. Mishchenko, V. I. Fal'ko, A. K. Geim, and A. I. Berdyugin, Long-range ballistic transport of Brown-Zak fermions in graphene superlattices, Nat. Commun. **11**, 5756 (2020).

[25] C. R. Dean, L. Wang, P. Maher, C. Forsythe, F. Ghahari, Y. Gao, J. Katoch, M. Ishigami, P. Moon, M. Koshino, T. Taniguchi, K. Watanabe, K. L. Shepard, J. Hone, and P. Kim, Hofstadter's butterfly and the fractal quantum Hall effect in moiré superlattices, Nature (London) **497**, 598 (2013).

[26] B. Hunt, J. D. Sanchez-Yamagishi, A. F. Young, M. Yankowitz, B. J. LeRoy, K. Watanabe, T. Taniguchi, P. Moon, M. Koshino, P. Jarillo-Herrero, and R. C. Ashoori, Massive Dirac Fermions and Hofstadter Butterfly in a van der Waals Heterostructure, Science **340**, 1427 (2013).

[27] C. R. Woods, L. Britnell, A. Eckmann, R. S. Ma, J. C. Lu, H. M. Guo, X. Lin, G. L. Yu, Y. Cao, R. V. Gorbachev, A. V. Kretinin, J. Park, L. A. Ponomarenko, M. I. Katsnelson, Yu. N. Gornostyrev, K. Watanabe, T. Taniguchi, C. Casiraghi, H.-J. Gao, A. K. Geim *et al.*, Commensurate–incommensurate transition in graphene on hexagonal boron nitride, Nat. Phys. **10**, 451 (2014).

[28] M. Andelković, S. P. Milovanović, L. Covaci, and F. M. Peeters, Double moiré with a twist: Supermoiré in encapsulated graphene, Nano Lett. **20**, 979 (2020).

[29] Z. Wang, Y. B. Wang, J. Yin, E. Tóvári, Y. Yang, L. Lin, M. Holwill, J. Birkbeck, D. J. Perello, S. Xu, J. Zultak, R. V. Gorbachev, A. V. Kretinin, T. Taniguchi, K. Watanabe, S. V. Morozov, M. Andelković, S. P. Milovanović, L. Covaci, F. M. Peeters *et al.*, Composite super-moiré lattices in double-aligned graphene heterostructures, Sci. Adv. **5**, eaay8897 (2019).

[30] X. Huang, L. Chen, S. Tang, C. Jiang, C. Chen, H. Wang, Z.-X. Shen, H. Wang, and Y.-T. Cui, Imaging dual-moiré lattices in twisted bilayer graphene aligned on hexagonal boron nitride using microwave impedance microscopy, Nano Lett. **21**, 4292 (2021).

[31] Y. Li, M. Xue, H. Fan, C.-F. Gao, Y. Shi, Y. Liu, K. Watanabe, T. Tanguchi, Y. Zhao, F. Wu, X. Wang, Y. Shi, W. Guo, Z. Zhang, Z. Fei, and J. Li, Symmetry breaking and anomalous conductivity in a double-moiré superlattice, Nano Lett. **22**, 6215 (2022).

[32] M. Long, Z. Zhan, P. A. Pantaleón, J. á. Silva-Guillén, F. Guinea, and S. Yuan, Electronic properties of twisted bilayer graphene suspended and encapsulated with hexagonal boron nitride, Phys. Rev. B **107**, 115140 (2023).

[33] T. Cea, P. A. Pantaleón, and F. Guinea, Band structure of twisted bilayer graphene on hexagonal boron nitride, Phys. Rev. B **102**, 155136 (2020).

[34] J. Shi, J. Zhu, and A. H. MacDonald, Moiré commensurability and the quantum anomalous Hall effect in twisted bilayer graphene on hexagonal boron nitride, Phys. Rev. B **103**, 075122 (2021).

[35] X. Lin and J. Ni, Symmetry breaking in the double moiré superlattices of relaxed twisted bilayer graphene on hexagonal boron nitride, Phys. Rev. B **102**, 035441 (2020).

[36] J. Shin, Y. Park, B. L. Chittari, J.-H. Sun, and J. Jung, Electron-hole asymmetry and band gaps of commensurate double moire patterns in twisted bilayer graphene on hexagonal boron nitride, Phys. Rev. B **103**, 075423 (2021).

[37] A. L. Sharpe, E. J. Fox, A. W. Barnard, J. Finney, K. Watanabe, T. Taniguchi, M. A. Kastner, and D. Goldhaber-Gordon, Evidence of orbital ferromagnetism in twisted bilayer graphene aligned to hexagonal boron nitride, Nano Lett. **21**, 4299 (2021).

[38] N. Bultinck, S. Chatterjee, and M. P. Zaletel, Mechanism for anomalous Hall ferromagnetism in twisted bilayer graphene, Phys. Rev. Lett. **124**, 166601 (2020).

[39] Y. H. Zhang, D. Mao, and T. Senthil, Twisted bilayer graphene aligned with hexagonal boron nitride: Anomalous Hall effect and a lattice model, Phys. Rev. Res. **1**, 033126 (2019).

[40] T. Fabian, M. Kausel, L. Linhart, J. Burgdörfer, and F. Libisch, Half-integer Wannier diagram and Brown-Zak fermions of

graphene on hexagonal boron nitride, Phys. Rev. B **106**, 165412 (2022).
[41] N. N. T. Nam and M. Koshino, Lattice relaxation and energy band modulation in twisted bilayer graphene, Phys. Rev. B **96**, 075311 (2017).
[42] R. Bistritzer and A. H. MacDonald, Moiré bands in twisted double-layer graphene, Proc. Natl. Acad. Sci. USA **108**, 12233 (2011).
[43] L. A. Chizhova, F. Libisch, and J. Burgdörfer, Graphene quantum dot on boron nitride: Dirac cone replica and Hofstadter butterfly, Phys. Rev. B **90**, 165404 (2014).
[44] R. Martinez-Gordillo, S. Roche, F. Ortmann, and M. Pruneda, Transport fingerprints at graphene superlattice Dirac points induced by a boron nitride substrate, Phys. Rev. B **89**, 161401(R) (2014).
[45] B. Sachs, T. O. Wehling, M. I. Katsnelson, and A. I. Lichtenstein, Adhesion and electronic structure of graphene on hexagonal boron nitride substrates, Phys. Rev. B **84**, 195414 (2011).
[46] C. Lei, L. Linhart, W. Qin, F. Libisch, and A. H. MacDonald, Mirror symmetry breaking and lateral stacking shifts in twisted trilayer graphene, Phys. Rev. B **104**, 035139 (2021).
[47] Y. Xie, A. T. Pierce, J. M. Park, D. E. Parker, E. Khalaf, P. Ledwith, Y. Cao, S. H. Lee, S. Chen, P. R. Forrester, K. Watanabe, T. Taniguchi, A. Vishwanath, P. Jarillo-Herrero, and A. Yacoby, Fractional chern insulators in magic-angle twisted bilayer graphene, Nature (London) **600**, 439 (2021).
[48] K. S. Novoselov, E. McCann, S. V. Morozov, V. I. Fal'ko, M. I. Katsnelson, U. Zeitler, D. Jiang, F. Schedin, and A. K. Geim, Unconventional quantum Hall effect and Berry's phase of 2π in bilayer graphene, Nat. Phys. **2**, 177 (2006).
[49] S. Engels, B. Terrés, A. Epping, T. Khodkov, K. Watanabe, T. Taniguchi, B. Beschoten, and C. Stampfer, Limitations to carrier mobility and phase-coherent transport in bilayer graphene, Phys. Rev. Lett. **113**, 126801 (2014).
[50] M. Schmitz, S. Engels, L. Banszerus, K. Watanabe, T. Taniguchi, C. Stampfer, and B. Beschoten, High mobility dry-transferred CVD bilayer graphene, Appl. Phys. Lett. **110**, 263110 (2017).
[51] J. Yu, B. A. Foutty, Z. Han, M. E. Barber, Y. Schattner, K. Watanabe, T. Taniguchi, P. Phillips, Z.-X. Shen, S. A. Kivelson, and B. E. Feldman, Correlated Hofstadter spectrum and flavour phase diagram in magic-angle twisted bilayer graphene, Nat. Phys. **18**, 825 (2022).
[52] R. Ribeiro-Palau, C. Zhang, K. Watanabe, T. Taniguchi, J. Hone, and C. R. Dean, Twistable electronics with dynamically rotatable heterostructures, Science **361**, 690 (2018).
[53] A. Uri, S. Grover, Y. Cao, J. A. Crosse, K. Bagani, D. Rodan-Legrain, Y. Myasoedov, K. Watanabe, T. Taniguchi, P. Moon, M. Koshino, P. Jarillo-Herrero, and E. Zeldov, Mapping the twist-angle disorder and landau levels in magic-angle graphene, Nature (London) **581**, 47 (2020).
[54] https://doi.org/10.5281/zenodo.10847164.
[55] W. Albrecht, J. Moers, and B. Hermanns, HNF - Helmholtz Nano Facility, J. Large-Scale Res. Facilities **3**, A112 (2017).
[56] J. M. Park, Y. Cao, K. Watanabe, T. Taniguchi, and P. Jarillo-Herrero, Flavour Hund's coupling, Chern gaps and charge diffusivity in moiré graphene, Nature (London) **592**, 43 (2021).
[57] K. Kim, M. Yankowitz, B. Fallahazad, S. Kang, H. C. P. Movva, S. Huang, S. Larentis, C. M. Corbet, T. Taniguchi, K. Watanabe, S. K. Banerjee, B. J. LeRoy, and E. Tutuc, van der Waals heterostructures with high accuracy rotational alignment, Nano Lett. **16**, 1989 (2016).
[58] D. Rhodes, S. H. Chae, R. Ribeiro-Palau, and J. Hone, Disorder in van der Waals heterostructures of 2D materials, Nat. Mater. **18**, 541 (2019).
[59] L. Wang, I. Meric, P. Y. Huang, Q. Gao, Y. Gao, H. Tran, T. Taniguchi, K. Watanabe, L. M. Campos, D. A. Muller, J. Guo, P. Kim, J. Hone, K. L. Shepard, and C. R. Dean, One-dimensional electrical contact to a two-dimensional material, Science **342**, 614 (2013).
[60] L. Banszerus, M. Schmitz, S. Engels, J. Dauber, M. Oellers, F. Haupt, K. Watanabe, T. Taniguchi, B. Beschoten, and C. Stampfer, Ultrahigh-mobility graphene devices from chemical vapor deposition on reusable copper, Sci. Adv. **1**, e1500222 (2015).
[61] A. Pierret, D. Mele, H. Graef, J. Palomo, T. Taniguchi, K. Watanabe, Y. Li, B. Toury, C. Journet, P. Steyer, V. Garnier, A. Loiseau, J.-M. Berroir, E. Bocquillon, G. Fève, C. Voisin, E. Baudin, M. Rosticher, and B. Plaçais, Dielectric permittivity, conductivity and breakdown field of hexagonal boron nitride, Mater. Res. Express **9**, 065901 (2022).
[62] A. Laturia, M. L. Van de Put, and W. G. Vandenberghe, Dielectric properties of hexagonal boron nitride and transition metal dichalcogenides: From monolayer to bulk, npj 2D Mater. Appl. **2**, 6 (2018).
[63] A. Schäpers, J. Sonntag, L. Valerius, B. Pestka, J. Strasdas, K. Watanabe, T. Taniguchi, L. Wirtz, M. Morgenstern, B. Beschoten, R. J. Dolleman, and C. Stampfer, Raman imaging of twist angle variations in twisted bilayer graphene at intermediate angles, 2D Mater. **9**, 045009 (2022).
[64] C. N. Lau, M. W. Bockrath, K. F. Mak, and F. Zhang, Reproducibility in the fabrication and physics of moiré materials, Nature (London) **602**, 41 (2022).
[65] E. Icking, L. Banszerus, F. Wörtche, F. Volmer, P. Schmidt, C. Steiner, S. Engels, J. Hesselmann, M. Goldsche, K. Watanabe, T. Taniguchi, C. Volk, B. Beschoten, and C. Stampfer, Transport spectroscopy of ultraclean tunable band gaps in bilayer graphene, Adv. Electron. Mater. **8**, 2200510 (2022).
[66] G. Kresse and J. Furthmüller, Efficient iterative schemes for ab initio total-energy calculations using a plane-wave basis set, Phys. Rev. B **54**, 11169 (1996).
[67] I. Souza, N. Marzari, and D. Vanderbilt, Maximally localized wannier functions for entangled energy bands, Phys. Rev. B **65**, 035109 (2001).
[68] A. A. Mostofi, J. R. Yates, G. Pizzi, Y.-S. Lee, I. Souza, D. Vanderbilt, and N. Marzari, An updated version of wannier90: A tool for obtaining maximally-localised wannier functions, Comput. Phys. Commun. **185**, 2309 (2014).
[69] N. Marzari and D. Vanderbilt, Maximally localized generalized wannier functions for composite energy bands, Phys. Rev. B **56**, 12847 (1997).
[70] P. Moon and M. Koshino, Electronic properties of graphene/hexagonal-boron-nitride moiré superlattice, Phys. Rev. B **90**, 155406 (2014).
[71] C. Lanczos, An iteration method for the solution of the eigenvalue problem of linear differential and integral operators, J. Res. Natl. Bur. Stand. **45**, 255 (1950).